

RESEARCH

Open Access



Piezoelectric-immunomodulatory electrospun membrane for enhanced repair of refractory wounds

Shu Liu^{1†}, Jiabin Yuan^{1†}, Maodan Nie^{2†}, Xumiao Lin¹, Xiongfei Li¹, Kai Luo¹, Shicheng Huo^{3*}, Yushu Bai^{1*} and Ningfang Mao^{1*}

Abstract

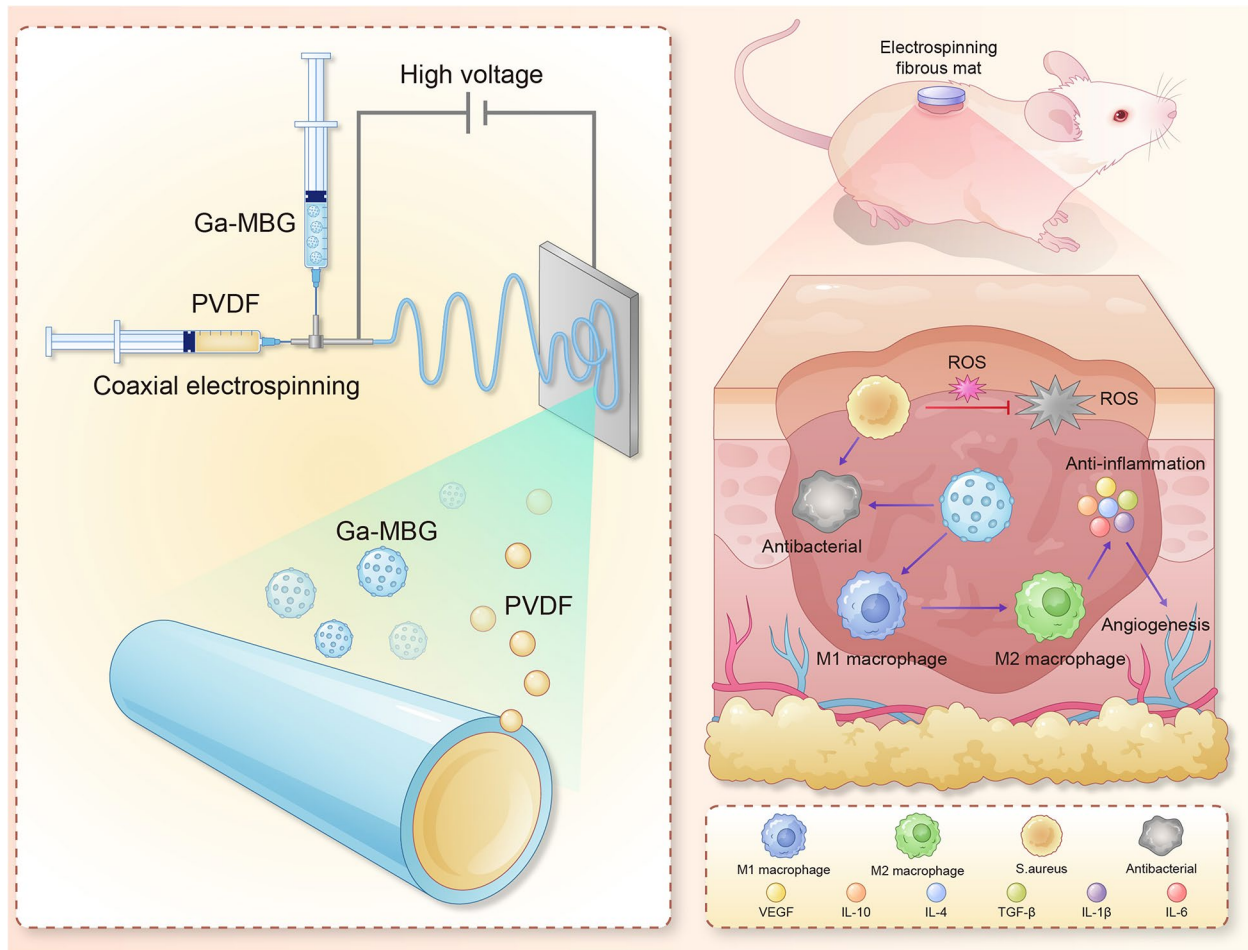
The microenvironment and healing process of diabetic wounds are highly complex, necessitating the development of wound dressings that combine excellent biocompatibility, superior antibacterial properties, and immune-regulating capabilities. However, achieving this goal remains a significant challenge. In this study, a multifunctional electrospun dressing (polylactic acid@Ga, PLLA@Ga) was designed and fabricated by integrating sonodynamic therapy with gallium-doped mesoporous bioactive glass (Ga-MBG). Compared to pure PLLA materials, PLLA@Ga exhibited remarkable antibacterial effects in vitro and demonstrated effective anti-infection properties in vivo. These effects are primarily attributed to the release of Ga ions, which competitively replace iron, thereby disrupting iron-dependent bacterial enzymes and ultimately leading to bacterial death. Additionally, in vitro experiments showed that PLLA@Ga could promote macrophage polarization from the M1 to M2 phenotype, effectively modulating the immune microenvironment of diabetic infected wounds. In vivo wound healing experiments further revealed that PLLA@Ga significantly enhanced collagen deposition and angiogenesis, accelerating the healing process of infected diabetic wounds. Thus, the multifunctional electrospun dressing developed in this study holds great potential as a promising candidate for the treatment of diabetic wounds.

[†]Shu Liu, Jiabin Yuan, and Maodan Nie contributed equally to this work.

*Correspondence:
Shicheng Huo
waznxyz@126.com
Yushu Bai
spinebaiys@163.com
Ningfang Mao
maonf@163.com

Full list of author information is available at the end of the article



Graphical abstract

Keywords Diabetic wounds, Ga-MBG, Electrospinning, Antibacterial, Macrophage

Introduction

The global prevalence of diabetes continues to rise, and diabetic wounds, as one of the common complications of diabetes, have a lifetime incidence rate of 19–34% [1, 2]. Diabetic wounds are often accompanied by persistent infections and healing difficulties. If not treated promptly or appropriately, they may lead to amputations, severely impairing patients' quality of life and health status, while significantly increasing societal healthcare costs [3, 4]. Therefore, achieving effective diagnosis and treatment of diabetic wounds remains a major challenge in the fields of public health and clinical medicine.

The persistent difficulty in healing diabetic wounds is typically due to a combination of factors, including ongoing bacterial infections, impaired angiogenesis of granulation tissue cells, disruption of the local immune environment, excessive wound exudate, and improper wound management [5, 6]. In clinical practice,

early treatment strategies for diabetic wounds primarily involve wound disinfection, exudate control, modulation of the local immune environment, promotion of angiogenesis, infection control, optimization of blood glucose management, and surgical debridement when necessary [7, 8]. Research indicates that regulating macrophage polarization during the inflammatory phase is crucial for diabetic wound healing [9, 10]. During the early inflammatory response, M1 macrophages play a role by secreting large amounts of pro-inflammatory cytokines to maintain the inflammatory state, while M2 macrophages are closely associated with the resolution of chronic inflammation, promoting tissue repair and wound healing through the secretion of anti-inflammatory cytokines [11, 12]. The dynamic balance between these macrophage subtypes is essential for the normal wound healing process.

Traditional wound dressings, such as hydrogels, foam dressings, and silver-containing dressings, exhibit significant limitations in the management of diabetic wounds [13–15]. These dressings struggle to fully meet the complex needs of diabetic wounds in terms of exudate absorption, maintaining wound moisture, preventing infection, and ensuring breathability. Moreover, they lack immunomodulatory functions and cannot accommodate the multi-stage requirements throughout the diabetic wound healing process, particularly in regulating inflammatory responses and promoting tissue repair, thereby limiting their clinical efficacy. For example, they may cause excessive moisture in diabetic wounds, insufficient breathability, and overly small pore sizes. Furthermore, the survival rate of cells within hydrogels is low, and cell migration is restricted, often leading to uneven cell distribution [16, 17]. This also limits the exchange of nutrients, oxygen, and metabolic waste within the hydrogel, thereby hindering its further clinical application to some extent.

A promising yet underexplored strategy is the integration of piezoelectric materials into wound dressings. Piezoelectricity enables the conversion of mechanical energy (e.g., ultrasound or physiological movements) into electrical signals, which can modulate cellular behaviors and enhance therapeutic outcomes. Recent studies demonstrated that piezoelectric materials promote ROS generation under ultrasound (US) for antibacterial therapy, while Huo et al. utilized piezoelectric materials to regulate immune responses [18, 19]. However, none of these works have combined piezoelectricity with bioactive ion release to achieve synergistic antibacterial, immunomodulatory, and pro-healing effects.

Electrospinning, due to its high porosity and suitable pore size, exhibits microstructural characteristics similar to skin [20]. Numerous studies have demonstrated that electrospun materials effectively prevent wound contamination, absorb exudates, and maintain a moist yet adequately breathable environment, thereby promoting wound healing [21–23]. Additionally, these materials provide a physical barrier to protect wounds from further damage and enhance tissue regeneration. Given its relatively simple fabrication process, electrospun materials are widely regarded as an ideal choice for wound dressings, holding significant potential for clinical applications. Nevertheless, simple electrospinning does not inherently possess immunomodulatory functions or antibacterial properties. Therefore, it is imperative to develop effective composite electrospinning techniques to endow it with both immunoregulatory and antibacterial activities. MBG exhibits unique bioactivity by modulating the extracellular matrix environment through the release of soluble degradation products, namely bioactive ions [24, 25]. Among various potential additives, Ga^{3+} have garnered increasing attention due to their excellent

biocompatibility and multifunctionality. Recent studies have demonstrated that Ga^{3+} possess significant anti-inflammatory and antibacterial properties. For instance, Yang et al. reported that Ga^{3+} alleviate chronic inflammation by inhibiting the release of inflammatory factors and promoting macrophage polarization towards the M2 phenotype [26]. Additionally, Ga^{3+} can competitively replace iron, thereby disrupting iron-dependent bacterial enzyme functions, ultimately leading to bacterial death [27, 28]. These characteristics make Ga-MBG a promising candidate material for promoting diabetic wound healing, with significant application prospects.

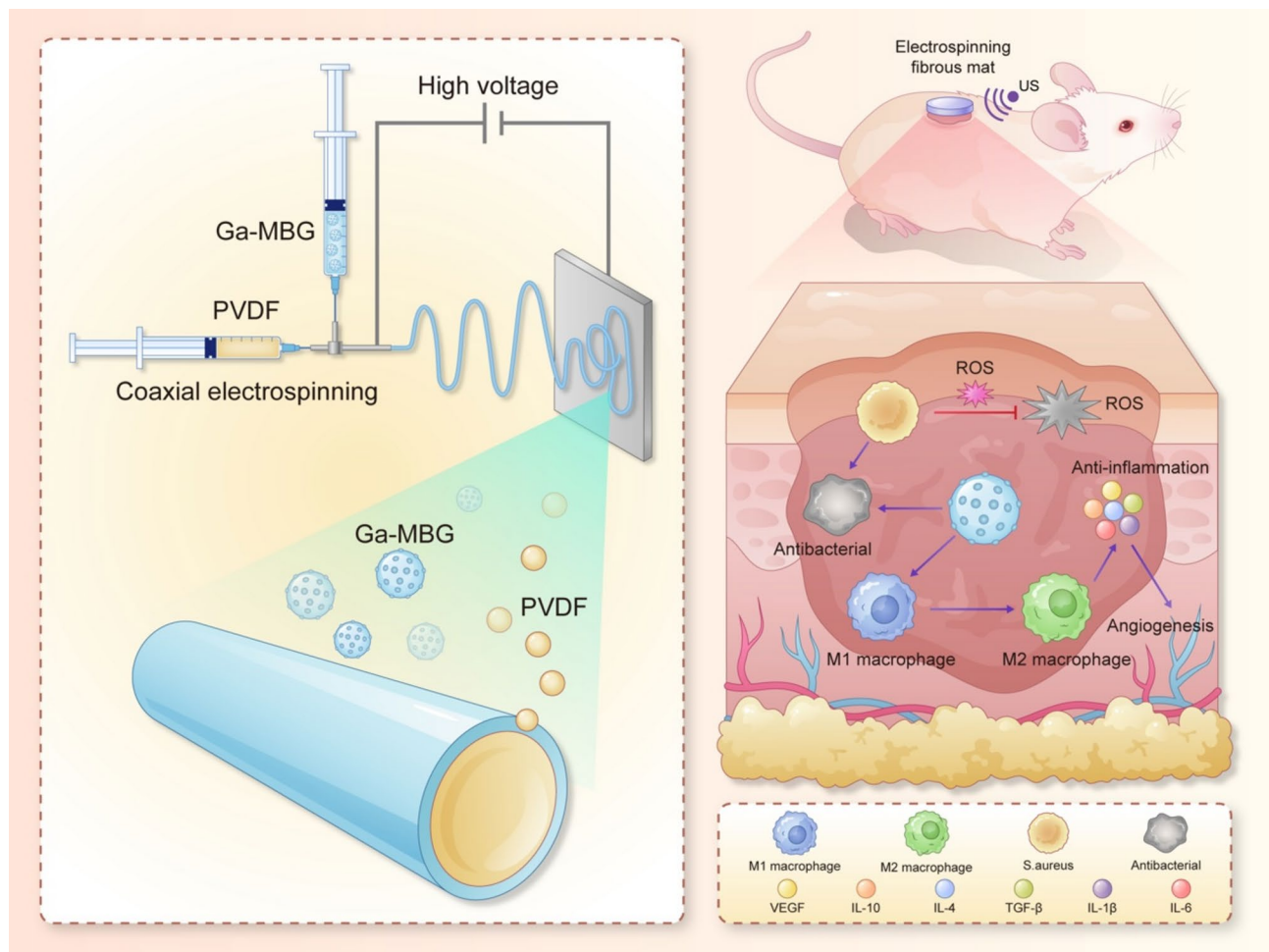
Hence, we propose an innovative PLLA@Ga composite material that combines the advantages of PLLA and Ga-MBG, while also introducing a piezoelectric effect to further enhance its potential applications in wound healing. Compared to traditional Ga-MBG, PLLA@Ga not only offers superior antibacterial properties and promotes cell adhesion but also provides additional mechanical stimulation through the piezoelectric effect, which modulates cellular behavior, promotes angiogenesis, and regulates immune responses, thereby accelerating wound healing. In contrast to electrospun dressings, the PLLA@Ga composite material presents a more comprehensive therapeutic strategy, featuring a robust supporting structure and biocompatibility, while also enhancing cellular activity through the electric field effect and stimulating the local repair processes of the wound environment. The synthesis process and functional mechanisms of the PLLA@Ga composite electrospinning are detailed in Scheme 1. In summary, this composite electrospun dressing demonstrates significant potential for clinical application in the treatment of diabetic infectious wounds.

Materials and methods

Synthesis and characterization

First, prepare a solution of PCL and hexafluoroisopropanol with a concentration of 10 wt%. Then, add 0.5 mg/mL of Ga-MBG to the PCL solution and stir overnight. Subsequently, draw the above solution with a 5 mL syringe and use an electrospinning device for spinning (PLLA@Ga). The spinning parameters are as follows: flow rate 1 mL/h, roller speed 2800 rpm, collector distance 15 cm, voltage (DC) 16 kV. The collected spun film is then placed in a vacuum drying oven for 6 h to allow for thorough evaporation.

Scanning electron microscope (SEM, Zeiss, Germany) was used to observe the morphology and elemental distribution of the spun filaments. The chemical composition and state of the spun film were analyzed using X-ray diffraction (XRD, Bruker, Billerica, MA, USA), X-ray photoelectron spectroscopy (XPS, ESCALAB 250Xi, Thermo Fisher, USA), and Fourier Transform Infrared Spectroscopy (FTIR, Magna-IR 750, Thermo Fisher, USA). The



Scheme 1 Synthesis process of PLLA@Ga and its mechanism for promoting diabetic wound healing. The preparation of PLLA@Ga involves electrospinning a solution of PLLA and Ga-MBG. Under US stimulation, the PLLA@Ga membrane enhances the production of ROS, thereby increasing antibacterial activity. Furthermore, PLLA@Ga promotes the polarization of macrophages from the M1 phenotype to the M2 phenotype, thereby modulating the immune microenvironment and accelerating wound healing

surface morphology and average roughness (R_a , the arithmetic mean deviation of surface roughness) of the samples were evaluated using a three-dimensional confocal laser scanning microscope (3D-CLSM, VK-X100K, Keyence, Osaka, Japan). The contact angles of water and diiodomethane were estimated with a contact angle goniometer (CAM, JC2000D1, Shanghai Zhongchen Digital Technology Instrument Co., Ltd., Shanghai, China), and the surface energy was calculated using the Owens-Wendt-Rabel-Kaelble (OWRK) equation [29]. The Piezo Force Microscope (PFM) utilizes the inverse piezoelectric effect of piezoelectric materials to detect the piezoelectric response of the materials. Under the stimulation of LIPUS, the output voltage of each set of samples was measured using a digital oscilloscope (DHO1000, China). The parameters were set as follows: center frequency 1 MHz, pressure intensity 30 mW/cm^2 , duty cycle 50%. Fenton piezoelectric process, we conducted EPR radical-trapping experiments and identified the contribution of

active species. We employed TBA as a quencher for $\bullet\text{OH}$ and DMPO (10 mM) as a radical-trapping agent, both at a concentration of 10 mM. The release profile of Ga^{3+} from PLLA@Ga was investigated using an inductively coupled plasma mass spectrometer (ICP-MS, Agilent 5110, USA), including assessments in phosphate-buffered saline (PBS) at varying pH levels (pH = 5.5 or pH = 7.4), as well as tests conducted in the presence or absence of US.

Ultrasound treatment

Each sample was subjected to US treatment using the Intellect Mobile Ultrasound (Chattanooga 2776, DJO Group, USA). For the piezoelectric catalytic performance test and antibacterial experiments, US parameters of 1.0 MHz, 1.5 W/cm^2 , and 50% duty cycle were employed, while experiments related to RAW 264.7 cells utilized US parameters of 1.0 MHz, 0.5 W/cm^2 , and 50% duty cycle. The ultrasound parameters (1.0 MHz, 1.5 W/cm^2 , 50% duty cycle) were established with reference to results

from existing studies, aiming to balance antibacterial efficiency with biological safety [30, 31].

In vitro cytocompatibility

The research employed human umbilical vein endothelial cells (HUVEC) and rat skin fibroblasts (RS-1) obtained from the American Type Culture Collection (ATCC). These cell types were cultivated in Dulbecco's modified Eagle's medium (DMEM, Gibco) supplemented with 10% fetal bovine serum (FBS) and 1% penicillin/streptomycin.

The biocompatibility of the composite PLLA@Ga was evaluated in vitro by directly culturing HUVEC and RS-1 cells (2×10^4 cells/well, 24-well plate) on various fibrous membranes for 24 h. After staining for live/dead cells, images were acquired using CLSM. The specific parameter settings were as follows: Calcein-AM (live cell staining, green fluorescence) was excited at a wavelength of 488 nm, with emission detected between 500 and 550 nm; Propidium Iodide (PI, dead cell staining, red fluorescence) was excited at 561 nm, with emission detected between 570 and 620 nm. A 20 \times objective lens was used for image acquisition, with a uniform exposure time set to 200 ms, and image processing and analysis were conducted using Leica LAS X software. For each experimental group, at least three random fields of view were selected for imaging to ensure data representativeness. Moreover, the proliferation of HUVEC and RS-1 cells when seeded on different fibrous membranes was determined using the CCK-8 assay. At days 1, 4, and 7 post-seeding, the medium was replaced, CCK-8 reagent was introduced, and cells were incubated for an additional 2 h, followed by measuring absorbance at 450 nm. Each experiment was conducted in triplicate.

The blood compatibility of different hydrogels was evaluated through hemolysis activity assessment. Initially, 500 μ L of rat blood was obtained and subjected to centrifugation at 3500 rpm for 5 min at 4 $^{\circ}$ C to isolate the red blood cell layer, which underwent additional centrifugation steps before being resuspended in 5 mL of PBS. Subsequently, 250 mg of hydrogel specimen was combined with 1 mL of red blood cells and left to incubate at room temperature for 4 h. To gauge hemolysis levels, both a negative control (PBS) and a positive control (distilled water) were included. Following centrifugation at 3000 rpm for 5 min, the absorbance at 545 nm was determined by measuring the supernatant of all samples.

In vitro antioxidant efficiency and tube formation

A total of 1×10^5 macrophages (cell density per membrane) were cultured on various composite membranes and exposed to H_2O_2 at a concentration of 100 μ M for 12 h. Subsequently, the generation of reactive oxygen species (ROS) was assessed within a 30-minute time-frame utilizing CLSM and flow cytometry in conjunction

with DCFH-DA staining at a concentration of 5 μ M. In the angiogenesis experiment, a mixture of matrix gel and conditioned medium at a 1:1 ratio was applied to a 96-well plate and allowed to solidify by incubating at 37 $^{\circ}$ C for 30 min. Subsequently, 1×10^4 HUVEC cells were seeded on the gel surface, and 300 μ L of different CM were added to each well. After an additional 3-hour incubation at 37 $^{\circ}$ C, live/dead cells were stained, and images were taken using a Leica DMI8 inverted fluorescence microscope. Cell culture supernatants were collected after the different treatments and levels of the cytokine VEGF were determined using an enzyme-linked immunosorbent assay (Elisa).

In vitro antibacterial activity

The frozen *Staphylococcus aureus* (*S. aureus*, ATCC[®] 25923[™]), *Escherichia coli* (*E. coli*, ATCC[®] 25922[™]), Methicillin-resistant *Staphylococcus aureus* (MRSA, ATCC[®] 43300[™]), and *Pseudomonas aeruginosa* (*P. aeruginosa*, ATCC[®] 27853[™]) cultures were thawed and subsequently incubated overnight in Tryptic Soy Broth (TSB) at 37 $^{\circ}$ C on a shaker. The resulting culture was then subjected to a 1:10000 dilution and further cultured until it reached the logarithmic phase of growth. In brief, the bacterial solution (500 μ L, 1×10^6 colony-forming units (CFU)/mL) was seeded on different fibrous membranes (For free gallium, we selected gallium nitrate ($Ga(NO_3)_3$) for evaluation, with a concentration comparable to that released by PLLA@Ga + US in a pH 5.5 environment over 24 h, approximately 8 mg/L). The antimicrobial activity of different spun membranes was investigated through live/dead staining analysis. Subsequently, the various bacteria were treated for 24 h following the aforementioned method, then diluted and inoculated onto agar plates using the spread plate method (SPM). After incubating for 18 h, photographs were taken, and the bacterial colony counts were recorded. The treated bacterial samples (including *S. aureus* and *E. coli*) were incubated with propidium iodide (PI) for a duration of 30 min. The stained solution was also analyzed using flow cytometry. Then, the fluorescence intensity of these samples was quantified utilizing a microplate reader, with the excitation and emission wavelengths set at λ_{ex} = 535 nm and λ_{em} = 615 nm, respectively.

In vitro antibacterial mechanism

We employed lysozyme sensitivity assay, alkaline phosphatase (AKP) test kit, and o-nitrophenyl- β -galactoside (ONPG) hydrolysis assay to assess the impact of various treatment methods on bacterial destruction. Initially, the bacteria (including *S. aureus* and *E. coli*) were subjected to different treatments. Subsequently, the culture medium was collected, and the supernatant was cultured using the AKP assay kit. The absorbance at 520 nm

(OD520) was then measured using a microplate reader. Next, the processed bacteria were collected and adjusted to an optical density (OD600) of 0.1 at 600 nanometers. Subsequently, the bacteria were cultured in NaH_2PO_4 buffer solution at pH 7 with lysozyme and ONPG solution at a concentration of 10 $\mu\text{g}/\text{mL}$. Finally, the absorbance at 600 nm and 420 nm was measured using a microplate reader. Additionally, to assess the extent of bacterial protein leakage, biofilms subjected to different treatments were collected. The bacterial supernatant was centrifuged at $8000 \times g$ for 10 min, and the absorbance at 260 nm (A260, nucleic acids) and 280 nm (A280, proteins) was measured using a microplate reader. All experimental procedures were performed in triplicate. To observe the ultrastructural changes of bacteria, processed bacteria samples are collected and fixed in a 2.5% glutaraldehyde solution at 4 °C for a minimum of 4 h. Subsequently, the samples are washed three times with PBS solution. Following this, a series of ethanol solutions with varying concentrations are used for dehydration, followed by infiltration with embedding medium and finally embedding. The embedded samples are sectioned into ultrathin slices, stained with uranyl acetate on grids, and observed under TEM. Moreover, the intracellular ROS levels of treated bacteria were evaluated by staining the bacteria with DCFH-DA and analyzing the samples via flow cytometry.

Cut PLLA@Ga into circular membranes with a diameter of 10 mm. Dilute a single colony of *S. aureus* grown in the logarithmic phase gradient with PBS solution to 1×10^6 CFU/mL. Place the samples in the center of a 48-well plate, adding 200 μL of bacterial suspension to each well. Incubate the samples and bacterial suspension at 37 °C for 1 h. After bacterial precipitation on the material, treat each sample under a 1.5 W/cm^2 ultrasonic device for 5 min. Collect the bacterial suspension from the wells, rinse the well walls and sample surfaces with 0.85% NaCl solution, transfer the samples and all bacterial suspensions to a 50 mL centrifuge tube, shake vigorously for 5 min, remove the samples, centrifuge the remaining liquid at 6000 rpm for 10 min, discard the supernatant, freeze the pellet with liquid nitrogen, and store temporarily in a -80 °C freezer. Then, the samples were placed in dry ice and sent to NovaGenomics (Beijing) Co., Ltd. for analysis using Illumina NovaSeq 6000. Gene Ontology and Kyoto Encyclopedia of Genes and Genomes were utilized for gene function analysis. Differential gene expression analysis was performed using edgeR (Robinson et al.), with genes meeting the criteria of $P < 0.05$ and $\log_2\text{FC} > 1$ considered as differentially expressed genes.

In vitro Immunomodulatory evaluation

In order to examine the immunomodulatory potential of PLLA@Ga in vitro, the analysis of surface markers (CD86 and CD206) on M1 and M2 macrophages was conducted through immunofluorescence staining and flow cytometry. Specifically, macrophages (1×10^5 /well) were seeded on different fibrous membranes, while a pro-inflammatory environment was induced with 100 ng/mL lipopolysaccharide (LPS). Immunofluorescence staining was performed on the cells following 24 h of culture. After fixation and blocking, the cells were treated with anti-CD206 and anti-CD86 antibodies, followed by the respective secondary antibodies. Subsequently, staining with DAPI was carried out, and visualization was done using CLSM. Quantification of CD206-positive and CD86-positive cells was conducted using ImageJ software. Changes in macrophage subtypes were then assessed through the utilization of CD86 and CD206 antibodies via flow cytometry. Following a 24-hour culture period, the supernatant was extracted, macrophages were harvested, rinsed with PBS, and labeled with CD206 and CD86 antibodies. Subsequently, the cells underwent washing and were suspended in 300 μL PBS for flow cytometry evaluation.

RNA sequencing was employed to examine the gene expression patterns of macrophages following treatment with PLLA@Ga. In summary, macrophages underwent the specified treatment protocol and were subsequently cultured for 24 h. Following incubation, macrophages treated with LPS and PLLA@Ga + US were lysed utilizing Trizol (Sigma) to isolate mRNA, which was subsequently subjected to sequencing. Each experimental group was represented by three biological replicates for mRNA sequencing analysis. To confirm the sequencing findings, the levels of quantitative inflammatory-related genes were measured and the release of inflammatory factors by macrophages following co-cultivation was evaluated. Macrophages were cultivated using the aforementioned method and RNA was isolated. The control gene ACTB was utilized for accurate gene expression analysis normalization. Detailed primer sequences can be found in the Supplementary Information (Table S1). Supernatants from macrophage cultures post various treatments were collected, and levels of cytokines (IL-1 β , TNF- α , IL-4, IL-10) were determined using Elisa.

Infected diabetic wound healing in vivo

All animal experiments conducted in this study were supervised and approved by Changhai Hospital. Male C57BL/6J mice aged 6–8 weeks were utilized to establish the type 1 diabetes model. Diabetes was induced using a standard protocol by intraperitoneal injection (i.p.) of STZ (30 mg/kg) for 7 consecutive days. Regular monitoring of body weight and blood glucose levels was

performed. Mice with fasting blood glucose levels ≥ 16.7 mmol/L after 4 weeks of STZ injection were considered diabetic. Diabetic mice were systematically allocated into five distinct groups ($n=12$): the control group, the US group, the PLLA group, the PLLA@Ga group, and the PLLA@Ga+US group. The mice underwent anesthesia with 2.5% TBE (200 mg/kg, intraperitoneally), followed by the complete removal of dorsal hair. Subsequently, a full-thickness wound was induced on the dorsal skin using an 8 mm diameter skin biopsy punch. To establish an infected wound model, 50 μ L of *S. aureus* solution (5×10^7 CFU/mL) was administered. Subsequently, wounds were treated with PBS (control), US, PLLA, PLLA@Ga, and PLLA@Ga+US, respectively. All wound groups were covered with Tegaderm film (1622 W, 3 M) to secure the composite membrane and prevent contamination, with digital images recorded every two days. After 14 days of treatment, all mice were euthanized with isoflurane, and wound tissues were collected for histological examination. Quantitative assessments of the histological sections will be performed to further elucidate the differences in healing efficacy among the treatment modalities. The biosafety of PLLA@Ga+US in vivo was evaluated by isolating major organs, such as the heart, spleen, lungs, liver, and kidneys. To further validate the systemic biosafety of the therapeutic strategy, we conducted blood biochemical analysis in mice.

Statistical analysis

All data are presented in the form of mean \pm standard deviation. Statistical analysis was conducted on the groups using one-way analysis of variance (ANOVA). A P-value less than 0.05 is considered statistically significant.

Results and discussion

Characterization

SEM and TEM were utilized to characterize the morphology and elemental composition of the synthesized Ga-MBG. As depicted in Fig. 1a, Ga-MBG appears as uniform spherical particles with an average diameter of approximately 100 nanometers, consistent with TEM observations. TEM images (Fig. 1b) reveal the uniform spherical morphology of Ga-MBG particles with an average diameter of approximately 100 nm. In addition, TEM image clearly shows the mesoporous structure of Ga-MBG. Energy-dispersive X-ray spectroscopy (EDS) mapping confirms the homogeneous distribution of Ga within the MBG framework, indicating successful doping of Ga ions. As demonstrated in Fig. 1c, the successful preparation of Ga-MBG loaded PLLA electrospun fibers resulted in the uniform distribution of Ga-MBG within the fibers. The FTIR spectrum of electrospun membranes is illustrated in Fig. 1d. The original PLLA FTIR

absorption spectrum displays C=O and C-O-C stretching vibrations at 1756 and 1182 cm^{-1} , respectively. Furthermore, the absorption band at 1045 cm^{-1} is linked to C-CH₃ stretching vibrations, while those at 1087 and 1130 cm^{-1} correspond to the symmetric stretching of C-O-C and CH₃ rocking modes, respectively [32–34]. In contrast, all composite spun membranes show characteristic absorption bands of PLLA. Notably, PLLA@Ga does not exhibit any distinct additional absorption bands compared to PLLA. This may be due to overlapping absorption bands between PLLA and PLLA@Ga, or possibly due to the very low content of nanofillers in the composite material. FTIR results suggest that the chemical structure of PLLA remains unchanged from its original state upon the addition of nanofillers. XRD analysis was conducted to investigate the structural characteristics of PLLA@Ga for further research purposes (Fig. 1e). The peaks observed at 19.7° (broad) and 16.6° were attributed to the 203 and 200/100 planes of PLLA, respectively [35]. The XRD pattern of the composite material revealed the absence of peaks corresponding to the nano filler (Ga-MBGs), suggesting that the nano filler is evenly dispersed within the PLLA matrix or present at a lower concentration compared to PLLA in the composite material. The XPS spectra of Ga 2p indicate that Ga-MBG are embedded within the internal framework of PLLA@Ga (Fig. 1f).

The three-dimensional microscopic images obtained using laser confocal microscopy were utilized to measure surface roughness (Fig. 1g-h). PLLA@Ga exhibited surfaces rougher than PLLA, consistent with the findings from the scanning electron microscopy images. WCA is utilized to determine the surface hydrophilicity of electrospun membranes. Studies have shown that various factors, including cell adhesion and protein absorption, are influenced by the hydrophilicity of biomaterials [36]. Therefore, biomaterials with appropriate hydrophilicity are crucial in a biological environment. In our research, the original PLLANF scaffold had a WCA of 95.8°, indicating that PLLA is hydrophobic (Fig. 1i-j). However, the WCA of the composite membrane incorporating Ga-MBG fibers decreased to 53.8°. Thus, the incorporation of Ga-MBG enhanced the hydrophilicity of the composite membrane, providing PLLA@Ga with improved biocompatibility in terms of cell proliferation and differentiation.

To quantify the surface energy of different samples, the contact angles of diiodomethane were measured (Fig. 1k), yielding values of 51.8°(PLLA) and 56.2° (PLLA@Ga). Furthermore, the surface energy of PLLA and PLLA@Ga samples were measured to be 31.35 and 46.98 mJ/m^2 , respectively (Fig. 1l). The surface energy of PLLA@Ga is significantly higher than that of pure PLLA, a change primarily attributed to the introduction of Ga-MBG, which enhances the hydrophilicity of the material. This increase in surface energy indicates that the PLLA@Ga composite

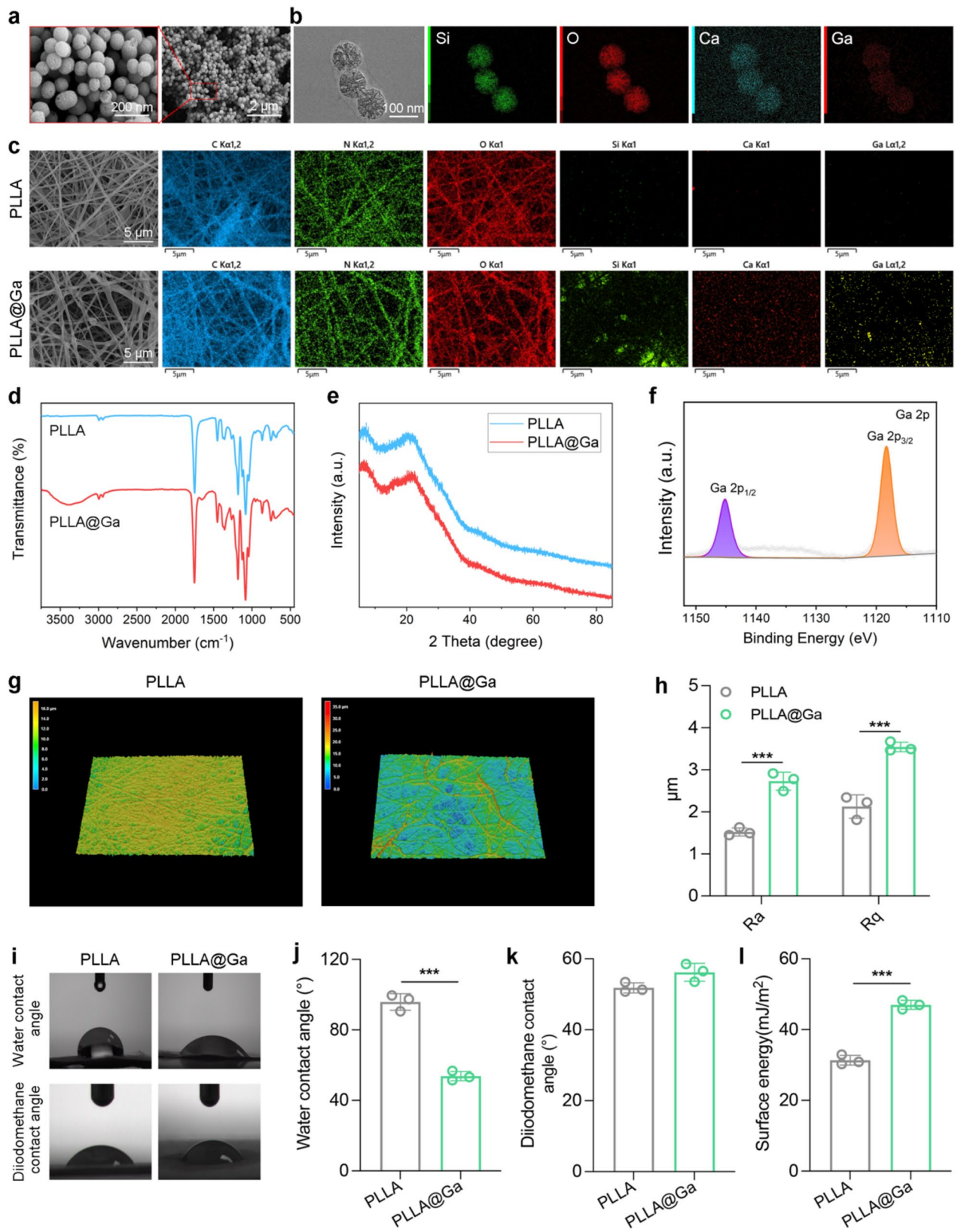


Fig. 1 Preparation and characterization of Ga-MBG and PLLA@Ga. **(a)** SEM images of Ga-MBG. **(b)** TEM and EDS images of Ga-MBG. **(c)** SEM and EDS mapping images of PLLA and PLLA@Ga. **(d)** FTIR of PLLA and PLLA@Ga. **(e)** XRD of PLLA and PLLA@Ga. **(f)** XPS of PLLA@Ga. **(g)** 3D-CLSM of PLLA and PLLA@Ga. **(h)** Surface roughness of PLLA and PLLA@Ga. **(i)** Water contact angle and diiodomethane contact angles of PLLA and PLLA@Ga. **(j)** Statistics on water contact angle of PLLA and PLLA@Ga. **(k)** Statistics on diiodomethane contact angles of PLLA and PLLA@Ga. **(l)** Surface energy of PLLA and PLLA@Ga

exhibits greater polarity and hydrophilicity in an aqueous environment, facilitating improved interactions with biomolecules, particularly the adsorption of proteins and the formation of the extracellular matrix (ECM). Research has shown that higher surface energy can provide a more favorable microenvironment for cells, thereby promoting cell adhesion, growth, and proliferation [37]. By facilitating the construction of the extracellular matrix, it can further enhance tissue functional recovery and repair. Moreover, high surface energy materials can also improve signal transduction between cells and the material, which is crucial for the tissue regeneration process. In the context of diabetic wound healing, effective signal transduction at the cell-material interface can promote cell activation and differentiation, thereby accelerating

the wound healing process. By modulating the energy state of the material's surface, the PLLA@Ga composite can effectively improve the wound microenvironment, leading to enhanced wound repair outcomes.

Therefore, based on its excellent surface energy characteristics and biocompatibility, the PLLA@Ga composite emerges as a highly suitable novel dressing for diabetic wound repair. This material can provide superior support for cell growth, offering an ideal therapeutic solution for wound healing in diabetic patients.

In the PFM mode of atomic force microscopy (AFM), a tip bias of 10 V was applied to conduct localized point-to-point piezoelectric response tests on the sample material, aimed at investigating the piezoelectric characteristics of the material's surface. Figure 2a illustrates the surface

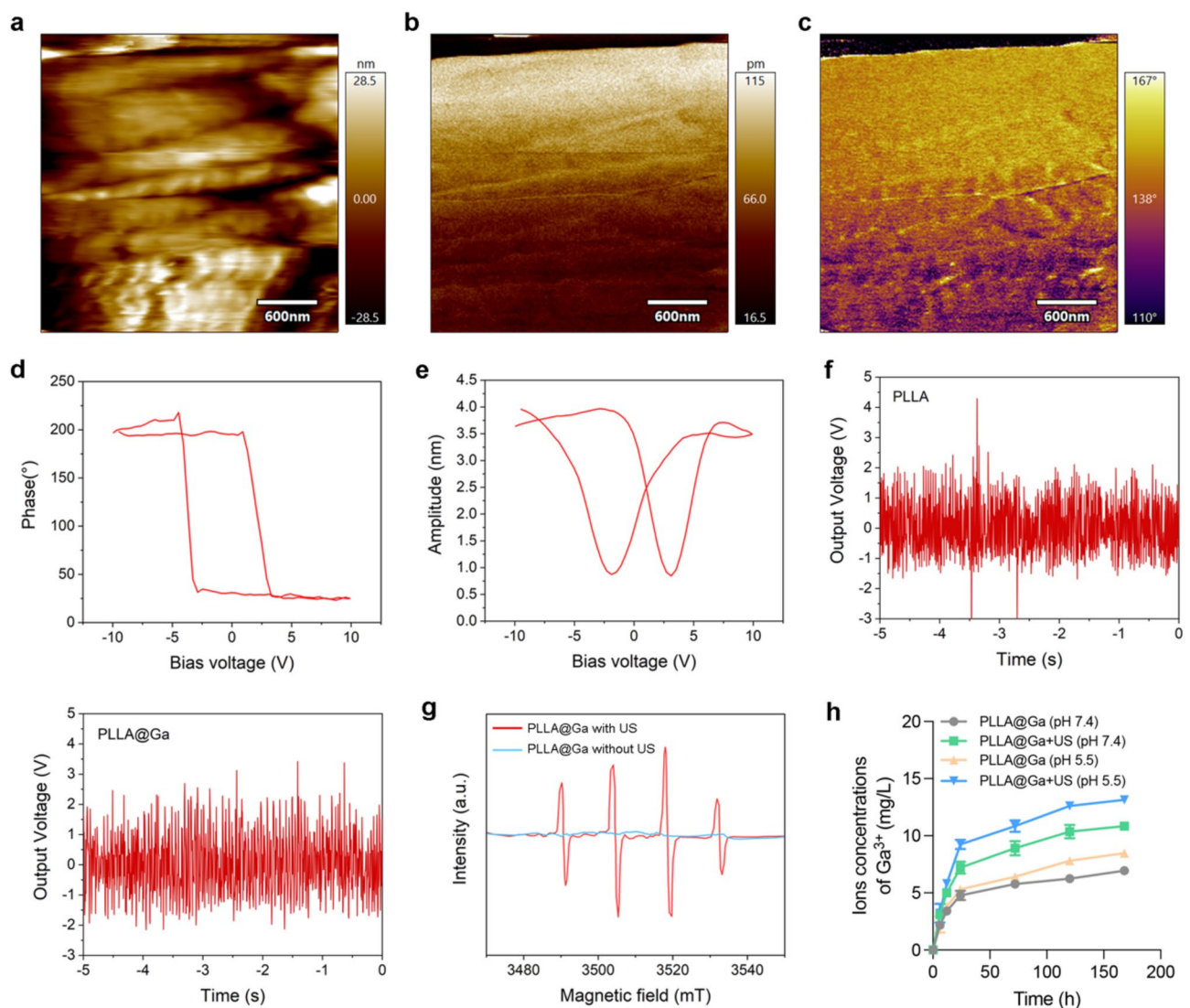


Fig. 2 Characterization of PLLA@Ga. **(a)** PFM image of PLLA@Ga material surface. **(b)** Piezoelectric amplitude of PLLA@Ga. **(c)** Phase angle of PLLA@Ga. **(d)** Butterfly cycle curve of PLLA@Ga. **(e)** Piezoelectric flip curve of PLLA@Ga. **(f)** The output voltage of PLLA@Ga under US stimulation. **(g)** ESR of PLLA@Ga with US or without US. **(h)** Ga^{3+} concentration was determined by ICP-OES after immersion of PLLA@Ga in PBS at different pH (pH 7.4 and pH 5.5) for different times with or without US

of the selected piezoelectric material. The experimental results presented in Fig. 2b-c indicate that the magnitude of the piezoelectric response on the material's surface, following the application of the tip bias, was 115 pm and a phase angle of 167° , respectively. This suggests that the material's surface exhibits a high piezoelectric response capability, further validating the exceptional piezoelectric properties of the PLLA@Ga composite material at the nanoscale. The characteristic hysteresis loop and pronounced butterfly curve observed in the PLLA@Ga samples in Fig. 2d-e reveal the material's spontaneous polarization ability under the influence of switching voltage, indicating favorable electrical behavior. Additionally, the material continues to demonstrate a robust piezoelectric effect under ultrasonic mechanical forces, showcasing inherent spontaneous polarization characteristics, thereby defining the material's non-zero remnant polarization or ferroelectric properties. These piezoelectric and polarization characteristics provide significant evidence for the material's potential applications in the biomedical field, particularly in diabetic wound healing.

To further validate the piezoelectric conversion capability of the prepared material, we tested its output voltage response under ultrasonic pressure. Figure 2f shows that both PLLA and PLLA@Ga exhibit distinct output voltage signals when subjected to dynamic US pressure, indicating that the material can effectively convert US energy into electrical energy, further confirming its excellent piezoelectric performance. In addition to the piezoelectric response tests, we also investigated the ability of PLLA@Ga to generate ROS under US stimulation. For this purpose, we employed electron spin resonance (ESR) spectroscopy to assess the generation of hydroxyl radicals ($\bullet\text{OH}$) under US stimulation. As shown in Fig. 2g, a prominent $\bullet\text{OH}$ characteristic peak was observed in the ESR spectrum, indicating that the PLLA@Ga composite material can effectively produce hydroxyl radicals under US stimulation. This suggests that PLLA@Ga undergo specific reactions under US stimulation, converting hydrogen peroxide (H_2O_2) into highly reactive $\bullet\text{OH}$ radicals, thereby further enhancing the material's antibacterial properties and promoting wound healing.

In summary, the experimental results indicate that the PLLA@Ga composite material not only possesses excellent piezoelectric performance but also enhances antibacterial effects through ROS generation under US stimulation. This broadens the application prospects of the material in diabetic wound healing, particularly in modulating immune responses, promoting wound repair, and preventing infections.

In this study, we immersed PLLA@Ga composites in PBS buffer solution ($\text{pH}=7.4$) and recorded the concentration changes of Ga^{3+} in the solution at different time points, both in the presence and absence of US, as

illustrated in Fig. 2h. Over the period from 6 h to 7 days, the concentration of gallium ions gradually increased, indicating that the PLLA@Ga material underwent an ion release process in the PBS solution. In comparative experiments, we observed that the Ga^{3+} release rate in the US (+) group was significantly higher than that in the US (-) group, with the total amount of Ga^{3+} at the end of the experiment also markedly greater in the US (+) group. This suggests that the application of ultrasound can effectively accelerate the release of Ga^{3+} from PLLA@Ga composites, likely due to mechanical effects induced by ultrasound that enhance the dissolution or diffusion rate of the ions. Furthermore, we investigated the impact of pH on Ga^{3+} release. Experimental results indicated that under lower pH conditions ($\text{pH}=5.5$), the release rate of Ga^{3+} from PLLA@Ga was significantly accelerated. This phenomenon may be related to the increased degradation rate of the material in an acidic environment, facilitating the leaching of Ga^{3+} from the composite. Given that wound sites often exhibit localized acidic conditions, particularly during the inflammatory phase or in the presence of bacterial infection, lower pH values may promote the release of more Ga^{3+} , thereby enhancing the antibacterial efficacy of the material.

In vitro effects of PLLA@Ga + US

The importance of good biocompatibility cannot be overstated in the clinical application of biomaterials. To assess this, we conducted in vitro biocompatibility testing on various materials using live/dead staining, CCK8, and hemolysis assays. Initially, HUVEC and RS1 cells were cultured on different spinnerets with or without ultrasound stimulation. Following a 24-hour incubation period, live/dead staining was performed. The results depicted in Fig. 3a illustrate that after the treatments, the majority of HUVEC and RS1 cells exhibited high viability (green fluorescence) with minimal cell death (red fluorescence). These findings suggest that PLLA@Ga demonstrates biocompatibility and supports cell survival. The impact of PLLA@Ga on cell proliferation was further examined through CCK8 analysis. The CCK-8 assay results demonstrated that cell proliferation increased over the course of 1, 4, and 7 days of culture, indicating that PLLA@Ga supports cell growth without cytotoxicity (Fig. 3b). Unlike the 1-day culture period, cell absorbance values increased after 4 and 7 days of culture with all treatments, suggesting that PLLA@Ga effectively enhances cell proliferation. Hemolysis experiments also confirmed the blood compatibility of PLLA@Ga, as none of the biomaterial treatments resulted in significant hemolysis (Fig. 3c). These findings highlight the favorable biocompatibility, non-hemolytic nature, and support for cell adhesion, growth, and proliferation provided by PLLA@Ga composite electrospinning.

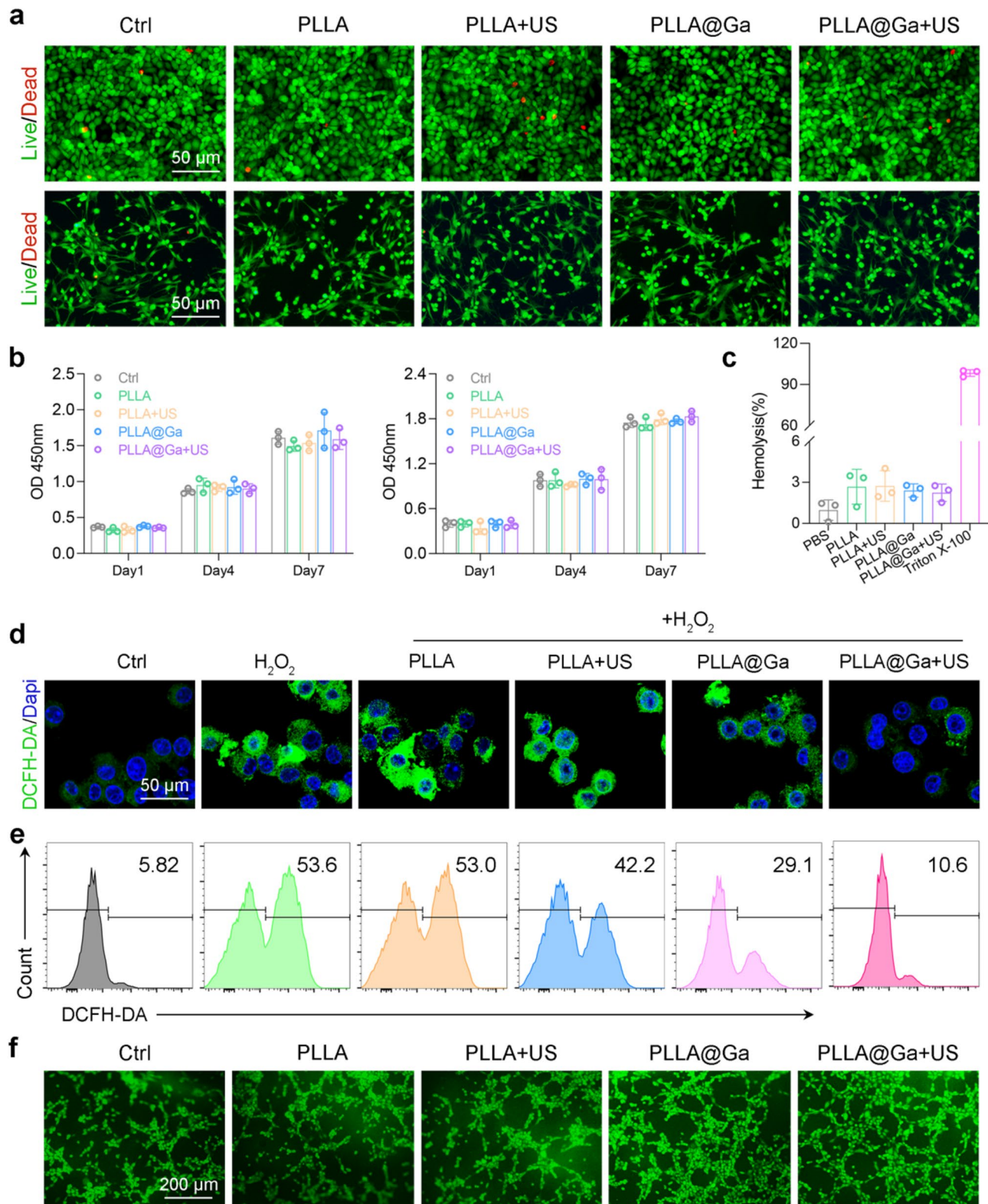


Fig. 3 Effects of PLLA@Ga + US in vitro. **(a)** Images of live/dead assays of HUVECs (upper panel) and RS-1 cells (lower panel). **(b)** CCK-8 assay of HUVECs (left panel) and RS-1 cells (right panel). **(c)** Hemolysis assay results of various materials exposure. **(d)** Fluorescence imaging was employed to assess the reduction of intracellular ROS in H_2O_2 -stimulated Raw264.7 cells. **(e)** Analysis of intracellular ROS in H_2O_2 -stimulated Raw264.7 cells after different treatments via flow cytometry. **(f)** Tube formation by coculturing HUVECs with various hydrogels

The typical characteristics of diabetic wounds include elevated levels of ROS, indicating that the wound is in a state of persistent oxidative stress. Immunofluorescence staining using DCFH-DA was employed to assess the ability of macrophages in the oxidative stress damage treatment group to clear intracellular. The control group exposed to H_2O_2 showed higher DCFH-DA staining, suggesting the induction of oxidative stress. Notably, after treatment with PLLA@Ga+US, the fluorescence signal decreased to levels similar to those of cells not exposed to H_2O_2 (Fig. 3d). The results are further supported by flow cytometry results (Fig. 3e). These findings suggest that PLLA@Ga+US can enhance the antioxidant capacity of macrophages by scavenging internal oxidants. Enhancing angiogenesis is crucial for tissue repair. Therefore, we employed the HUVEC tube formation assay to evaluate the impact of PLLA@Ga+US treatment on angiogenesis. The experimental results demonstrated a significant increase in the tubular network in the PLLA@Ga+US group compared to the control group (as shown in Fig. 3f), indicating that this treatment effectively promotes endothelial cell tube formation and the angiogenic process. The enhanced tube formation capability serves as a hallmark of endothelial cell migration, proliferation, and differentiation during angiogenesis, providing robust evidence for vascular reconstruction in the wound healing process. Furthermore, to validate the angiogenic potential of PLLA@Ga+US, we measured the secretion levels of vascular endothelial growth factor (VEGF) across different treatment groups using Elisa (Figure S2). VEGF is a crucial factor that promotes angiogenesis by stimulating endothelial cell proliferation and the formation of new blood vessels. The results revealed that the secretion levels of VEGF in the PLLA@Ga+US group were significantly higher than those in the control group, further substantiating the efficacy of this treatment in promoting angiogenesis.

The observed increase in cell proliferation and high cell viability on PLLA@Ga membranes is consistent with previous studies demonstrating the biocompatibility of Ga-doped materials. For instance, Li et al. reported that Ga^{3+} enhance cell adhesion and proliferation by modulating the extracellular matrix environment [38]. Additionally, the improved hydrophilicity of PLLA@Ga, as evidenced by the reduced water contact angle, aligns with findings from Sun et al., who highlighted that hydrophilic surfaces promote cell attachment and growth [39]. The antioxidant capacity of PLLA@Ga, as demonstrated by the reduction in intracellular ROS levels, is also supported by studies showing that Ga^{3+} can scavenge ROS and mitigate oxidative stress [40]. These results collectively suggest that PLLA@Ga not only supports cell proliferation but also creates a favorable microenvironment for tissue regeneration." The enhanced tube formation observed

in the HUVEC assay indicates that PLLA@Ga promotes angiogenesis, a critical factor in diabetic wound healing. This finding is particularly significant given the impaired angiogenesis typically associated with diabetic wounds.

Antibacterial efficacy of PLLA@Ga + US

Dressings possessing potent antimicrobial properties are effective in safeguarding against pathogenic bacterial contamination, a critical factor influencing the progression of wound healing. The antibacterial effectiveness of PLLA@Ga+US electrospun fibers was assessed by testing them against various bacteria. The bacterial colonies were quantified post various treatments using SPM. As depicted in Fig. 4a and c, and S1, the bacterial colony count significantly decreased following the PLLA@Ga+US treatment. The bacteria subjected to various treatments were stained using live/dead staining and examined under a fluorescence microscope. The findings illustrated in Fig. 4b reveal a substantial increase in bacterial mortality (red fluorescence) within the PLLA@Ga+US group in comparison to other treatments, accompanied by a notable decrease in the number of surviving bacteria (green fluorescence). These outcomes underscore the potent antibacterial effectiveness of PLLA@Ga+US.

Subsequently, PI staining was employed to assess the bactericidal capability of PLLA@Ga+US (Fig. 4d). For *S. aureus*, the PI fluorescence intensity of the PLLA@Ga+US group increased by 9.45-fold, 9.13-fold, 1.26-fold, 0.76-fold, and 0.64-fold compared to the control group, PLLA group, PLLA+US group, PLLA@Ga group, and $Ga(NO_3)_3$ group (Fig. 4e), respectively. Similarly, for *E. coli*, the PI fluorescence intensity of the PLLA@Ga+US group increased by 9.89-fold, 9.13-fold, 1.41-fold, 0.87-fold, and 0.72-fold relative to the control group, PLLA group, PLLA+US group, PLLA@Ga group, and $Ga(NO_3)_3$ group (Fig. 4e), respectively. This indicates that the PLLA@Ga+US treatment can significantly disrupt bacterial cell membranes, enhancing their permeability. Furthermore, quantitative analysis of PI fluorescence intensity using a microplate reader corroborated the results obtained from the aforementioned flow cytometry (Fig. 4f). The results showed a significant correlation between PLLA@Ga+US treatment and increased PI fluorescence intensity, highlighting its potential as an effective antibacterial strategy.

Antibacterial efficacy of PLLA@Ga + US

Furthermore, the antibacterial effect of PLLA@Ga+US was further investigated by assessing the extracellular AKP content and ONPG hydrolysis assay. Following treatment with PLLA@Ga+US, there was a significant increase in extracellular AKP concentration (Fig. 5a), indicating damage to the bacterial cell wall. This

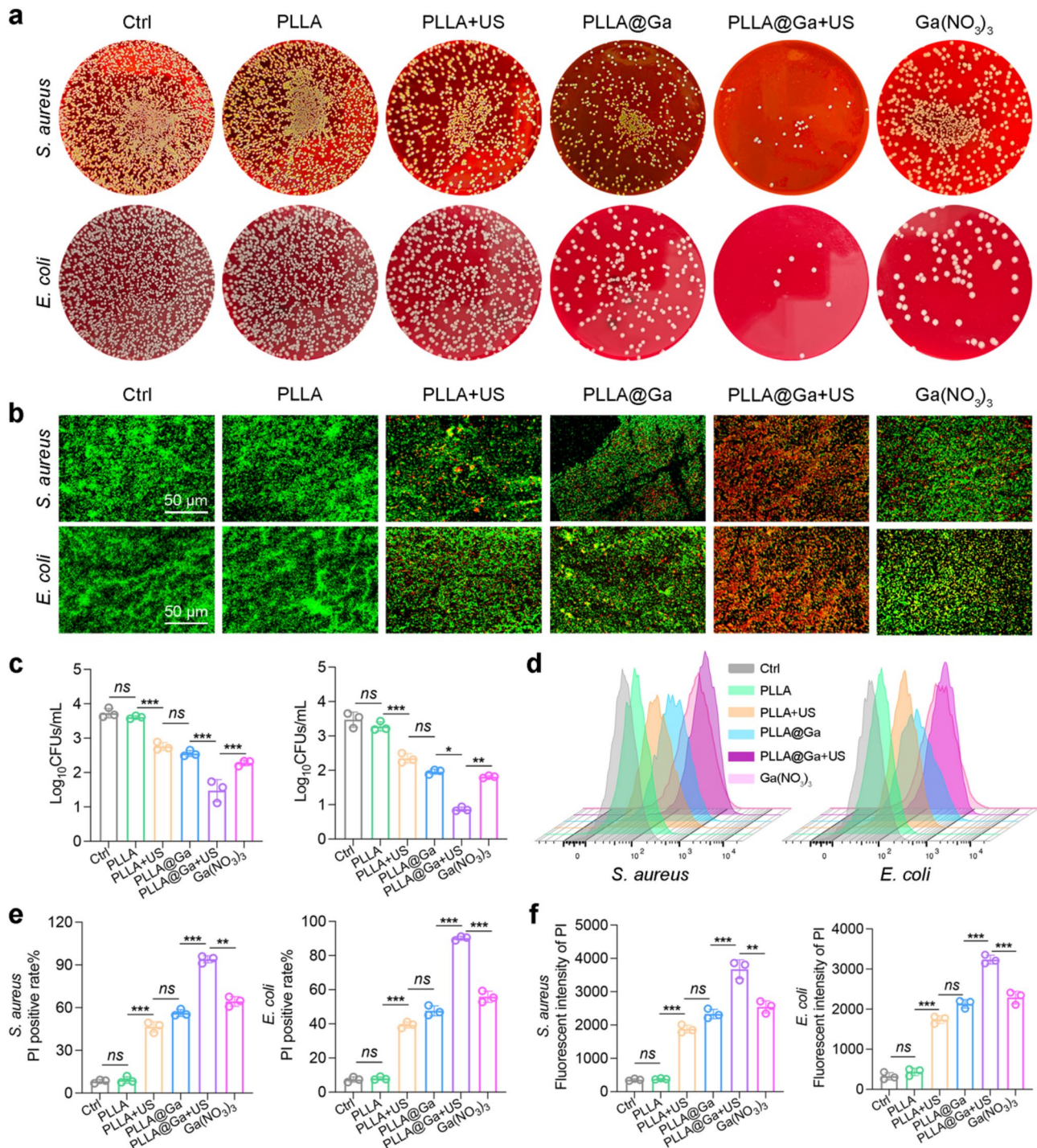


Fig. 4 In vitro antibacterial activity of PLLA@Ga + US. **(a)** Representative plates of bacteria colonies after treatment with different samples. **(b)** The fluorescence images of live (green) and dead bacterial (red). **(c)** Results of bacteria treated with various materials that formed colonies after 24 h. **(d-e)** Representative flow cytometry plots and quantitative analysis of PI. **(f)** Detection of membrane damage in bacteria through monitoring PI influx. Data are presented as mean \pm SD ($n = 3$). "ns" represent "no significant"; * $P < 0.05$; ** $P < 0.01$; *** $P < 0.001$

discovery suggests that this therapy is capable of effectively disrupting the bacterial cell wall. ONPG enters the cytoplasm and is subsequently hydrolyzed by cytoplasmic β -galactosidase, indicating an increase in bacterial

cell membrane permeability. Notably, the absorbance at 420 nm significantly increased following PLLA@Ga + US treatment (Fig. 5b), suggesting enhanced bacterial cell membrane permeability. Compared to other groups,

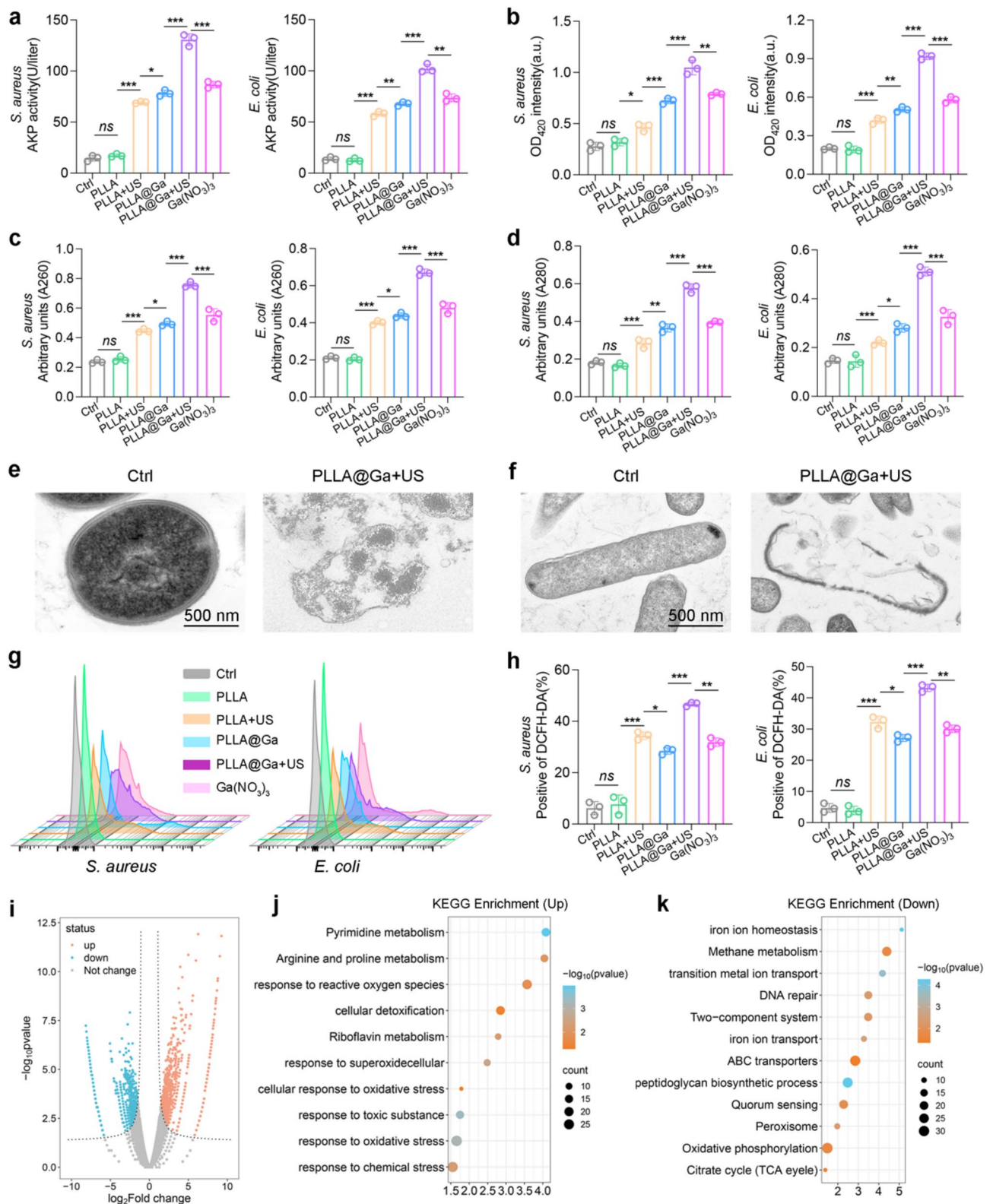


Fig. 5 In vitro antibacterial activity of PLLA@Ga + US. **(a)** The sensitivity to alkaline phosphatase activity. **(b)** The ONPG hydrolysis activity. **(c-d)** Leakage of cell contents after exposure to various treatments was investigated by monitoring the absorbance of extracellular material at 260 nm (A260) and 280 nm (A280) corresponding to nucleic acids and proteins, respectively. **(e-f)** Morphology of bacteria from different treatment groups as observed by TEM. **(g)** Assessment of ROS generation was conducted using DCFH-DA fluorescent probes by FCM. **(h)** Assessment of ROS generation was conducted using DCFH-DA fluorescent probes by microplate reader. **(i)** Volcano map of differentially expressed genes (DEGs). **(j-k)** KEGG pathway enrichment analysis. Data are presented as mean \pm SD ($n = 3$). "ns" represent "no significant"; * $P < 0.05$; ** $P < 0.01$; *** $P < 0.001$

bacteria treated with PLLA@Ga+US exhibited a significant increase in nucleic acid and protein absorbance at 260 nm and 280 nm (Fig. 5c-d). These results demonstrate that PLLA@Ga+US treatment can significantly alter bacterial membrane permeability, leading to cytoplasmic leakage. Furthermore, TEM results revealed that bacteria treated with PLLA@Ga+US showed contracted, blurred, and corrugated cell membranes, whereas the control group displayed smooth, intact, and well-defined cell membranes (Fig. 5e).

Subsequently, the potential mechanism of PLLA@Ga+US sterilization was investigated. According to previous studies, piezoelectric materials can produce a large amount of ROS under ultrasonic stimulation. Therefore, we speculate that this treatment may exhibit antibacterial properties through ROS activity. As shown in Figs. 5g–h, bacteria treated with PLLA@Ga+US exhibited a significant increase in ROS production. Therefore, ROS plays an integral role in the mechanism of PLLA@Ga+US sterilization. Furthermore, as per previous reports, Ga³⁺ possesses antibacterial activity primarily because bacteria absorb Ga and bind it to iron-dependent enzymes [41, 42]. However, Ga³⁺ is unable to be reduced under physiological conditions, rendering Ga-substituted enzymes unable to carry out the tasks of their iron-dependent counterparts, which are essential for bacterial growth. Since bacteria cannot differentiate between the two, they are unable to reduce their intake of Ga³⁺, as doing so would also decrease their intake of iron. Therefore, the potent bactericidal effect of PLLA@Ga+US can be attributed to the significant amount of Ga³⁺ disrupting bacterial iron metabolism and ultimately leading to bacterial death.

Next, RNA sequencing analysis was conducted on surviving *S. aureus* to identify gene expression differences between the control group and the PLLA@Ga-treated group under US treatment. Volcano plots were produced to visually represent the differentially expressed genes observed between the Ctrl group and the PLLA@Ga+US group (Fig. 5i). Utilize the KEGG enrichment method to analyze differentially expressed genes. In the PLLA@Ga+US group, genes associated with ROS, superoxide, and oxidative stress were significantly upregulated (Fig. 5j), indicating that PLLA@Ga+US treatment can enhance oxidative stress in *S. aureus*. Previous studies have shown that Ga³⁺ can bind to bacterial cytochromes, inhibiting the electron transfer of cytochrome-bound oxygen, leading to ROS production and inducing bacterial death [43]. Therefore, PLLA@Ga+US may inhibit bacterial growth by enhancing bacterial oxidative stress. In addition, pathways related to DNA repair are significantly downregulated in the PLLA@Ga+US group (Fig. 5k). This suggests that DNA repair is effectively inhibited, catalytic reactions within the bacteria are

disrupted, and bacterial morphological regulation is suppressed. Genes related to iron ion transport were significantly downregulated in the PLLA@Ga+US group (Fig. 5k), which can be explained by the bacteria's inability to distinguish between Ga³⁺ and Fe³⁺, resulting in the uptake of a large amount of Ga³⁺ [44]. Iron is one of the most crucial nutrients for bacteria, involved in essential intracellular redox and electron transfer processes. Consequently, PLLA@Ga+US can inhibit bacterial growth by interfering with *S. aureus*'s iron metabolism.

These results indicate that PLLA@Ga+US can inhibit the iron ion transport of *S. aureus*, reduce the activity of bacterial antioxidant enzymes, and amplify the oxidative stress of bacteria, thereby enhancing the antibacterial activity of PLLA@Ga during the SDT process.

Macrophage behavior

Numerous research findings indicate that the efficiency of wound healing is closely tied to the local inflammatory reaction within the tissue [45–47]. Undoubtedly, the immune system significantly influences this intricate process. Overactive or dysregulated immune responses can worsen tissue damage and impede the healing process. Hence, optimal wound healing and restoration transpire within a harmonious and well-regulated immune environment. Macrophages are recognized for their crucial involvement in the immune system and have the ability to transform into two distinct phenotypes, M1 (pro-inflammatory subtype) and M2 (pro-repair subtype), depending on the stimuli they encounter. M1 macrophages encourage the development of an inflammatory microenvironment through the secretion of various pro-inflammatory cytokines, including tumor necrosis factor- α (TNF- α), IL-6, and IL-1 β . Conversely, M2 macrophages facilitate tissue repair by releasing cytokines like IL-4, CD206, and IL-10 to establish an anti-inflammatory setting [48, 49]. The significance of this polarization is paramount, as the appropriate polarization of M1 and M2 macrophages greatly improves the tissue repair process. Conversely, excessive activation and polarization can worsen inflammation and hinder efficient wound healing [50]. Undoubtedly, the host immune response is a crucial factor in the wound healing process facilitated by biomaterials. Given the critical nature of these immune responses, our focus now shifts to investigating the immunomodulatory impacts of PLLA@Ga+US and its potential to enhance wound healing through modulation of macrophage activities.

Macrophages were seeded on different fibrous membranes for 24 h under LPS-induced inflammation. The immunomodulatory effect of PLLA@Ga+US was evaluated by analyzing the expression of macrophage M1 and M2 subtype markers through immunofluorescence staining. Results depicted in Fig. 6a revealed that after

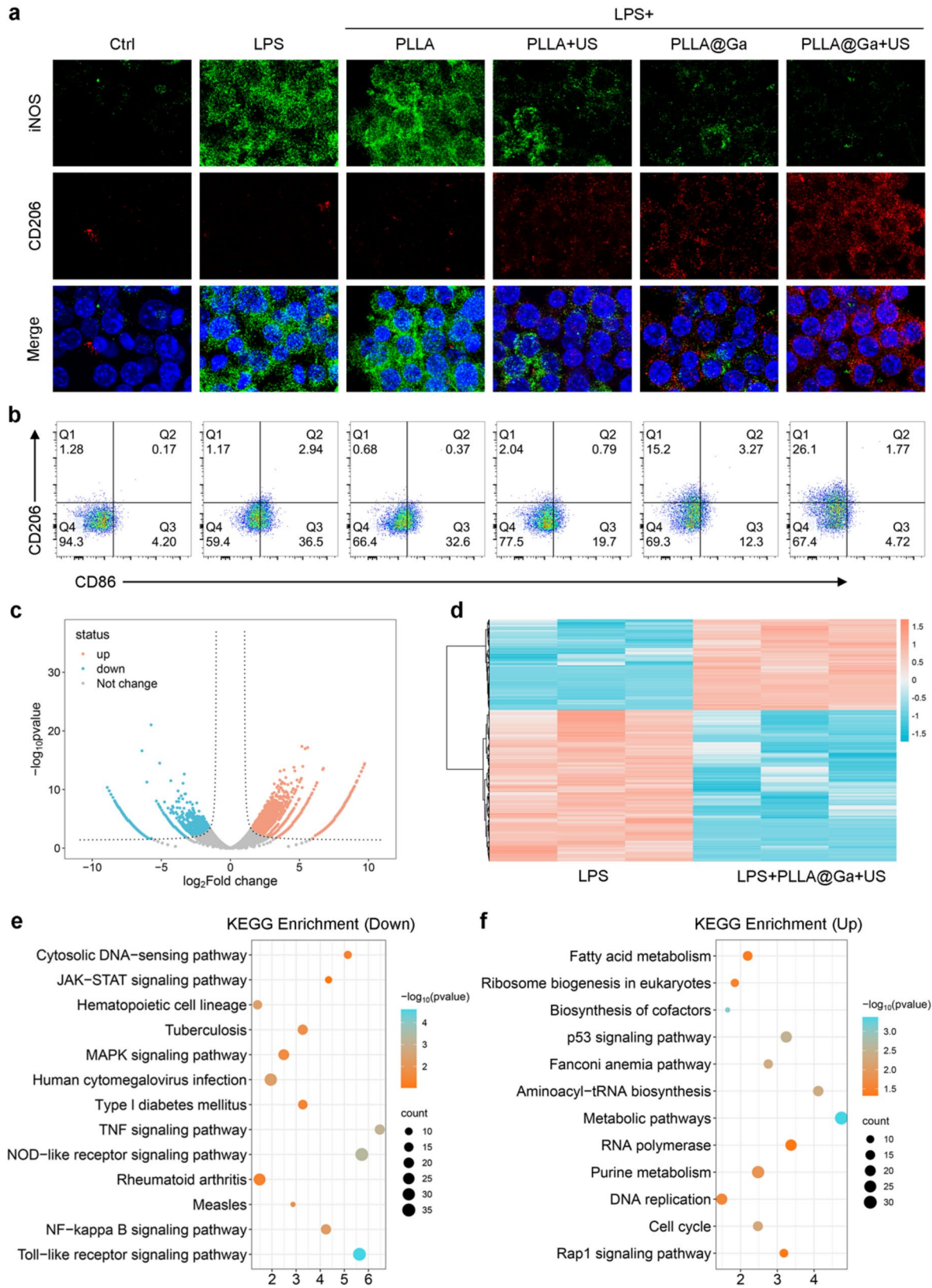


Fig. 6 Studies on the in vitro immunomodulatory of PLLA@Ga + US. **(a)** Expression of iNOS and CD206 following different hydrogel treatments. **(b)** Analysis of CD86 and CD206 in macrophages following various treatments via flow cytometry. **(c)** Volcano map of differentially expressed genes (DEGs). **(d)** Heat map of differentially expressed genes (DEGs). **(e)** KEGG enrichment for the down-regulated pathways. **(f)** KEGG enrichment for the up-regulated pathways

exposure to LPS, macrophages exhibited elevated levels of iNOS (green fluorescence). Conversely, treatment with PLLA+US, PLLA@Ga, and PLLA@Ga+US, particularly the latter, significantly decreased iNOS expression, suggesting an inhibitory effect on its expression (Figure S3a). Furthermore, the fluorescence intensity of CD206 notably increased following treatments with PLLA+US, PLLA@Ga, and PLLA@Ga+US compared to LPS treatment. Notably, PLLA@Ga+US exhibited the most pronounced effect on CD206 fluorescence intensity (Figure S3b). These findings indicate that PLLA@Ga+US has the potential to counteract the LPS-induced inflammatory microenvironment, suppressing macrophage M1 polarization while promoting M2 polarization.

The impact of different treatments on macrophage polarization was subsequently evaluated through flow cytometry analysis. The results revealed a significant decrease in the percentage of CD86-positive cells (M1 marker) and a notable increase in CD206-positive cells (M2 marker) following treatment with PLLA+US, PLLA@Ga, and PLLA@Ga+US, particularly PLLA@Ga+US. Specifically, the distribution of CD86-positive cells in the control, LPS, LPS+PLLA, LPS+PLLA+US, LPS+PLLA@Ga, and LPS+PLLA@Ga+US groups were 4.20%, 36.5%, 32.6%, 19.7%, and 12.3%, and 4.72%, respectively, while the proportions of CD206-positive cells were 1.28%, 1.17%, 0.68%, 2.04%, 15.2%, and 26.1% (Fig. 6b). These outcomes suggest a close relationship between PLLA@Ga+US treatment and the shift of macrophages towards the anti-inflammatory M2 phenotype. The downregulation of CD86 and upregulation of CD206 highlight the ability of PLLA@Ga+US to direct macrophages towards the reparative M2 subtype, which is vital for effective wound healing in cases of infection.

Furthermore, an in-depth investigation into the effects of PLLA@Ga+US on macrophages was conducted using RNA-Seq. Differentially expressed genes (DEGs) were identified with a p-value of less than 0.05 and a fold change (FC) greater than 2. The volcano plot in Fig. 6c vividly illustrates the substantial number of DEGs between the PLLA@Ga+US treatment group and the LPS group. The heatmap constructed based on these differential genes highlights the changes in gene expression between the LPS group and the LPS+PLLA@Ga+US group (Fig. 6d). KEGG pathway enrichment analysis further revealed specific signaling pathways associated with macrophage phenotype transformation (Fig. 6e-f). The analysis indicated that after PLLA@Ga+US treatment, inflammatory pathways related to M1 macrophage polarization, including MAPK signaling pathway, TOR-like receptor signaling pathway, NF-kappa B signaling pathway, and Nod-like signaling pathway, were significantly inhibited. In addition, upregulation of anti-inflammatory pathways was observed, particularly those associated

with M2 macrophage polarization, such as the TGF- β signaling pathways. This change in gene expression suggests that macrophages may be reprogrammed towards a more reparative phenotype, thereby promoting tissue regeneration.

To validate the RNA-Seq findings, the impact of PLLA@Ga+US treatment on the expression of inflammation-related genes in macrophages was examined using qPCR. After 24 h of culture, the expression levels of typical M1 macrophage markers (including IL-1 β , TNF- α , and iNOS) in the PLLA@Ga+US treatment group were found to be significantly lower compared to those in the LPS treatment group alone (Figure S1c). Conversely, the expression level of the M2 macrophage marker IL-10 showed a significant increase, which aligns with the RNA-Seq results. Elisa was employed to measure the secretion of inflammatory factors. The PLLA@Ga+US treatment demonstrated a significant decrease in the secretion levels of pro-inflammatory cytokines like IL-1 β and TNF- α (Figure S1d). These findings provide additional evidence supporting the ability of PLLA@Ga+US treatment to modulate macrophage transformation towards the anti-inflammatory subtype. These findings highlight the therapeutic potential of PLLA@Ga+US in modulating macrophage behaviour, thereby influencing the overall inflammatory response and promoting a healing-favourable microenvironment.

The characteristics of macrophages are influenced by various factors such as their inducers, properties, and surface markers. This research involved the creation of electrospun PLLA@Ga with piezoelectric capabilities to investigate its impact on macrophage phenotype. The findings indicated that applying PLLA@Ga with ultrasonic stimulation resulted in a reduction of M1-type macrophages induced by LPS, while promoting an increase in M2-type macrophages. By comparing with ICP results, we found that the concentration of Ga ions in PLLA@Ga is 11.74 mg/L. Previous studies have demonstrated that free Ga ions can inhibit the expression of inflammatory genes [51], indicating that Ga ions play an indispensable role in the anti-inflammatory effects of PLLA@Ga. Additionally, several research has shown that the piezoelectric effect induced by gentle US also possesses certain anti-inflammatory properties [30], which has been further confirmed in this study.

In vivo wound healing of PLLA@Ga+US

In the context of diabetes-related wounds, prolonged delays in healing pose a heightened risk of bacterial infection, thereby impairing the body's immune response and impeding the wound recovery process. This scenario can potentially escalate to severe infections and critical health complications [52, 53]. Hence, expediting the wound healing process is crucial for both preventing and

managing infections. This research delves into exploring the impact of PLLA@Ga on wound healing within an infected diabetic mouse model. Mice were induced with diabetes by injecting STZ and creating a 10 mm full-thickness wound on mice with blood glucose levels exceeding 16.65 mmol/L, followed by contamination with bacteria. Wounds treated with saline (control group),

PLLA, PLLA + US, PLLA@Ga, and PLLA@Ga + US were photographed and evaluated on days 0, 4, 7, 10, 14, 17, and 21. As shown in Fig. 7a-b, wounds treated with PLLA@Ga + US healed faster compared to other treatment groups. The healing rates of wounds treated with PLLA@Ga + US on days 4, 7, 10, 14, 17, and 21 were 21.5%, 36.9%, 48.2%, 57.373%, and 93.7% respectively,

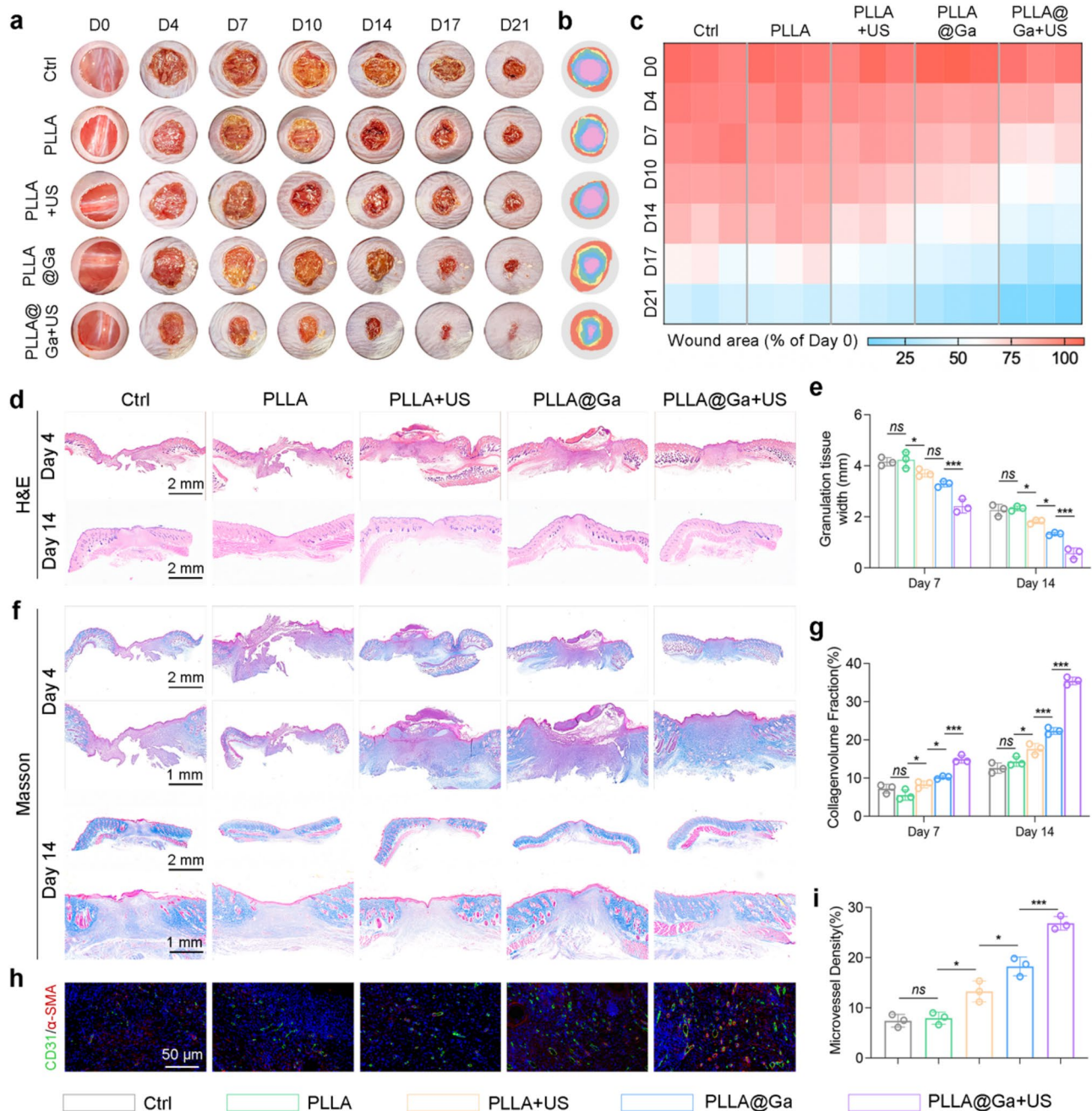


Fig. 7 PLLA@Ga+US promotes diabetic wound healing. (a-b) Photographs of wounds at predetermined time points and superimposed images of wounds after various treatments. (c) Areas of unhealed wounds in each group at different time intervals. (d) H&E staining. (e) Corresponding quantitative analysis of the granulation tissue width. (f) Masson's trichrome staining. (g) Statistical analysis of collagen deposition during the remodeling phase. (h) Representative immunofluorescence staining of microvessel of wound. (i) Statistical analysis of microvessel density. Data are presented as mean ± SD (n = 3). "ns" represent "no significant"; *P < 0.05; ***P < 0.001

while the control group only achieved a healing rate of 65.2% on day 21 (Fig. 7c).

On the 7th and 21st day post-operation, histological examination of the infected wound skin was conducted using H&E and Masson's trichrome staining for tissue analysis. Quantitative assessment of granulation tissue length, as shown in Fig. 8d-e, indicated a significantly accelerated wound contraction rate in the PLLA@Ga+US treatment group compared to the others. Adequate collagen deposition is crucial for tissue strength and healing during the remodeling process. We employed Masson's trichrome staining to evaluate new collagen. By day 21, the control group still had residual scabs, indicating delayed healing (Fig. 8f). In contrast, wounds treated with PLLA@Ga+US exhibited a clear red epidermal layer and more collagen. Furthermore, PLLA@Ga+US treatment also enhanced chronic wound healing, promoting effective regeneration of dermal appendages (Fig. 8g). In conclusion, the study findings suggest that PLLA@Ga+US treatment enhances the healing rate of infection-related diabetic wounds compared to other groups. Research findings indicate that successful wound healing relies on angiogenesis to provide crucial nutrients and oxygen. Thus, sufficient angiogenesis plays a vital role in the wound healing process [54]. The study assessed the presence of neoangiogenic markers, specifically cell adhesion molecule 1 (CD31) and α -smooth muscle actin (α -SMA), in sections of mouse skin wounds (Fig. 8h-i). The results revealed notably elevated levels of CD31 and α -SMA in wounds treated with PLLA@Ga+US, underscoring their noteworthy potential for promoting wound healing.

The effective treatment for diabetic infected wounds involves not only rapidly eradicating bacteria but also reversing the inflammatory response in the diabetic microenvironment. Histological analysis indicates that PLLA@Ga+US treatment can achieve rapid healing of diabetic infected wounds. In vitro experiments demonstrate that PLLA@Ga+US treatment can inhibit macrophage M1 polarization and promote M2 polarization. Therefore, it is reasonable to speculate that PLLA@Ga+US treatment can reverse the inflammatory microenvironment of diabetic wounds in vivo, thereby promoting wound healing. Collect wounds subjected to different treatments and analyze the single-cell suspensions using flow cytometry to quantify macrophage populations. Figure 8a-c demonstrate that, compared to other treatment groups, the PLLA@Ga+US treatment group exhibited fewer M1-like macrophages (CD86⁺CD206⁻) and a significant increase in M2-like macrophages (CD86⁻CD206⁺). Immunofluorescence staining of tissue-associated M1 (CD86) and M2 (CD206) macrophages revealed that PLLA@Ga+US treatment significantly enhanced M2 macrophage markers while reducing the expression of

M1 macrophage markers (Fig. 8d-f). These findings confirm that PLLA@Ga+US treatment improves the local immune microenvironment of diabetic infected wounds by decreasing CD86⁺ M1 macrophages and increasing CD206⁺ M2 macrophages near the wound, which is more conducive to wound healing. Moreover, PCR and Elisa were employed to quantify the gene expression and protein secretion levels of M1 cell factors (related to the pro-inflammatory marker IL1 β) and M2 cell factors (anti-inflammatory and angiogenesis markers IL10, TGF β 1, and VEGF) (Fig. 8g-h). The analysis results revealed a significant decrease in M1 macrophages factor expression levels and an increase in M2 macrophages factor protein levels in the PLLA@Ga+US treatment group, surpassing other treatment groups. These findings indicate that PLLA@Ga+US can effectively promote the healing of diabetic infected wounds.

Macrophages play a crucial role in the immune response to tissue damage. In diabetic wound infections, the transition of macrophages from an inflammatory (M1) to an anti-inflammatory (M2) state is disrupted, impeding wound healing [55, 56]. Our in vitro and in vivo studies demonstrate that PLLA@Ga+US effectively reduces the number of M1 macrophages while increasing the number of M2 macrophages, thereby enhancing the expression of anti-inflammatory and angiogenic cytokines, including IL-10, VEGF, and TGF- β 1. Specifically, IL-10 is a cytokine that alleviates inflammation and inhibits oxidative processes. Vascular endothelial growth factor plays a critical role in recruiting endothelial cells, thereby initiating angiogenesis. Additionally, TGF- β 1 recruits endothelial cells and fibroblasts to the wound site, promoting the synthesis of ECM [57]. In conclusion, PLLA@Ga+US shows significant potential in accelerating the healing of diabetic-infected wounds. By effectively modulating macrophage phenotypes, PLLA@Ga+US aids in suppressing inflammation response, promoting angiogenesis, and tissue remodeling.

In this study, we evaluated the effects of PLLA+US treatment on major organs, including the heart, liver, spleen, lungs, and kidneys, through H&E staining. The results indicated that none of these organs exhibited significant toxic responses following PLLA@Ga+US treatment (Figure S4). Specifically, the staining images did not reveal any tissue damage, inflammation, or other toxic characteristics. The tissue architecture of the heart, liver, spleen, lungs, and kidneys remained intact, with normal cellular morphology and no evident cellular infiltration or tissue destruction. Furthermore, the blood biochemical parameters of mice, such as total protein (TP), albumin (ALB), globulin (GLO), total bilirubin (TBIL), alanine aminotransferase (ALT), aspartate aminotransferase (AST), urea, and glucose (GLU), showed no significant changes after different treatments (Figure S5), indicating

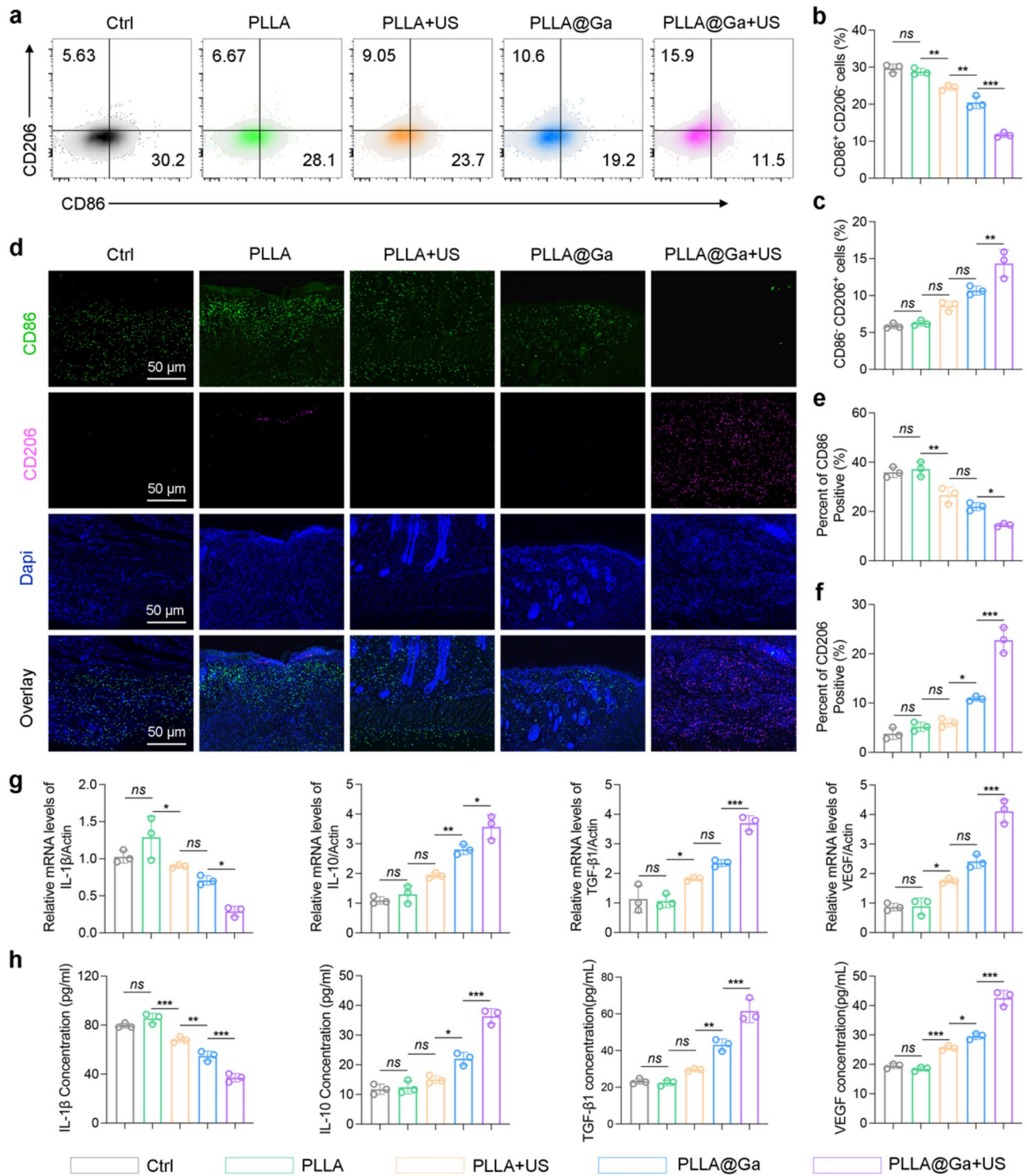


Fig. 8 Impact of the PLLA@Ga+US on macrophage polarization in vivo. **(a-c)** Flow cytometry of M1 and M2 macrophages retrieved from the wound tissue. **(d)** Immunofluorescence staining of tissue sections at the wound site for CD86 and CD206. **(e-f)** Statistical analysis concerning the proportion of CD86 **(f)** and CD206 **(g)** positive macrophages. **(g)** Gene expression levels of IL-1β, IL-10, VEGF, and TGF-β1 in wound tissues. **(h)** Secretion of IL-1β, IL-10, VEGF, and TGF-β1 in wound tissues assessed by Elisa. Data are presented as mean ± SD (n=3). "ns" represent "no significant"; *P<0.05; **P<0.01; ***P<0.001

that PLLA@Ga + US possesses excellent biocompatibility and biosafety. These findings suggest that PLLA@Ga + US treatment demonstrates good biocompatibility with these vital organs and does not elicit toxic responses, thereby providing a safety assurance for its clinical application. Furthermore, the ultrasound treatment did not cause any damage to the organs, further validating that the combined action of PLLA composites and ultrasound can promote wound healing while maintaining systemic safety.

Despite the promising *in vitro* and *in vivo* results, several challenges remain for the clinical translation of PLLA@Ga. These include the scalability of the electrospinning process, the long-term stability of the piezoelectric properties, and the potential need for repeated ultrasound treatments in clinical settings. Additionally, the safety and efficacy of PLLA@Ga in human patients need to be rigorously evaluated through clinical trials. It is important to note that while PLLA@Ga shows promising results, its performance should be contextualized within the broader field of advanced wound dressings. For instance, silver-based dressings and hydrogels have been widely used for their antibacterial properties, while growth factor-loaded scaffolds have shown efficacy in promoting angiogenesis [58–60]. Compared to these materials, PLLA@Ga offers a unique combination of piezoelectricity and Ga ion release, which may provide synergistic benefits in modulating the immune microenvironment and promoting tissue repair. However, further studies are needed to directly compare the efficacy of PLLA@Ga with these existing materials.

Conclusion

This study presents the development process of composite electrospun wound dressings with intrinsic immunomodulatory properties. The integration of piezoelectric properties into PLLA@Ga represents a promising approach to enhance wound healing, particularly in the context of diabetic wounds. While the concept of piezoelectric materials in biomedical applications is not entirely new, the combination of piezoelectricity with Ga-MBG for diabetic wound healing has not been extensively explored. Our results demonstrate that the piezoelectric effect of PLLA@Ga, when combined with US stimulation greatly enhances bacterial clearance and significantly enhances ROS generation and macrophage polarization, leading to improved wound healing outcomes. In conclusion, the developed composite electrospun material, PLLA@Ga + US, effectively modulates the immunoregulatory function of macrophages, showcasing substantial potential in repairing diabetic infected wounds and treating other immune-related diseases.

Supplementary Information

The online version contains supplementary material available at <https://doi.org/10.1186/s12951-025-03393-z>.

Supplementary Material 1

Acknowledgements

Not applicable.

Author contributions

LS, YJ, and NM designed the experiments. LS and NM performed the synthesis and characterization of the materials. LS and YJ performed the *in vitro* experiments. LX and LK participated in the *in vivo* experiments. LX, HS, LS, and MN contributed to data analysis. LS and MN contributed to the manuscript preparation. All authors read and approved the final manuscript.

Funding

This research was supported by the Shanghai Municipal Commission of Economy and Informatization, Health Commission, and Medical Insurance Bureau Application Demonstration Project (No. 23SH502200-05 and No. 23SH504700-08).

Data availability

No datasets were generated or analysed during the current study.

Declarations

Ethics approval and consent to participate

The procedures involving the animals and their care were conducted in conformity with national and international laws and policies. The animal experiments were approved by Changhai Hospital.

Consent for publication

All authors agreed with the publisher to publish this work.

Competing interests

The authors declare no competing interests.

Author details

¹Department of Spine Surgery, Changhai Hospital, Navy Military Medical University, 168 Changhai Road, Shanghai 200433, China

²School of Biomedical Engineering, Shanghai Jiao Tong University, No. 1954 Huashan Road, Xuhui District, Shanghai 200030, China

³Department of Orthopedic Surgery, Spine Center, Changzheng Hospital, Navy Medical University, Shanghai, China

Received: 23 November 2024 / Accepted: 15 April 2025

Published online: 06 May 2025

References

- Chokshi T, Fickweiler W, Jangolla S, Park K, Wu IH, Shah H, Sun JK, Aiello LP, King GL. Reduced Aqueous Retinol-Binding Protein 3 Concentration Is Associated With Diabetic Macular Edema and Progression of Diabetic Retinopathy. *Diabetes Care* (2024).
- Kuo S, Ye W, Wang D, McEwen LN, Villatoro Santos C, Herman WH. Cost-Effectiveness of the National Diabetes Prevention Program: A Real-World, 2-Year Prospective Study. *Diabetes Care* (2024).
- Chu Z, Liu X, Zhao T, Jiang D, Zhao J, Dong X, Yeung KWK, Liu X, Liao Y, Ouyang L. Self-healing Ppy-hydrogel promotes diabetic skin wound healing through enhanced sterilization and macrophage orchestration triggered by NIR. *Biomaterials*. 2024;315:122964.
- Zhang X, Ning F, Li Y, Lu J, He Y, Feng C, Dong CM. Pluripotent polysaccharide coordinated hydrogels remodel inflammation, neovascularization and reepithelization for efficient diabetic wound prohealing. *J Control Release*. 2024;377:37–53.
- Pu C, Wang Y, Xiang H, He J, Sun Q, Yong Y, Chen L, Jiang K, Yang H, Li Y. Zinc-based polyoxometalate nanozyme functionalized hydrogels for optimizing

- the Hyperglycemic-Immune microenvironment to promote diabetic wound regeneration. *J Nanobiotechnol.* 2024;22(1):611.
6. Zhou H, Chen L, Huang C, Jiang Z, Zhang H, Liu X, Zhu F, Wen Q, Shi P, Liu K, Yang L. Endogenous electric field coupling Mxene sponge for diabetic wound management: haemostatic, antibacterial, and healing. *J Nanobiotechnol.* 2024;22(1):530.
 7. Bernatchez SF. Current state of science in negative pressure wound therapy. *Adv Wound Care (New Rochelle)* (2024).
 8. Liao Y, Zhang Z, Zhao Y, Zhang S, Zha K, Ouyang L, Hu W, Zhou W, Sun Y, Liu G. Glucose oxidase: an emerging multidimensional treatment option for diabetic wound healing. *Bioact Mater.* 2025;44:131–51.
 9. Li J, Wu D, Su Z, Guo J, Cui L, Su H, Chen Y, Yu B. Zinc-induced photocross-linked Konjac Glucomannan/glycyrrhizic acid hydrogel promotes skin wound healing in diabetic mice through immune regulation. *Carbohydr Polym.* 2025;348:1122780. (Pt A).
 10. Zhang W, Li Y, Wei Y, Jiang Y, Hu Z, Wei Q. Antibacterial carboxymethyl Chitosan hydrogel loaded with antioxidant cascade enzymatic system for immunoregulating the diabetic wound microenvironment. *Int J Biol Macromol* (2024) 137539.
 11. Huang L, Li T, Geng W, Xie X, Wang P, Deng Y, Gao Y, Bai D, Tang T, Cheng C. Oxygen-Bonded Amorphous Transition Metal Dichalcogenides with pH-Responsive Reactive Oxygen Biocatalysis for Combined Antibacterial and Anti-inflammatory Therapies in Diabetic Wound Healing. *Small* (2024) e2407046.
 12. Yang P, Ju Y, Shen N, Zhu S, He J, Yang L, Lei J, He X, Shao W, Lei L, Fang B. Exos-Loaded Gox-Modified Smart-Response Self-Healing hydrogel improves the microenvironment and promotes wound healing in diabetic wounds. *Adv Healthc Mater* (2024) e2403304.
 13. Deng P, Shi Z, Fang F, Xu Y, Zhou LA, Liu Y, Jin M, Chen T, Wang Y, Cao Y, Su L, Liang H, Liu Q. Wireless matrix metalloproteinase-9 sensing by smart wound dressing with controlled antibacterial nanoparticles release toward chronic wound management. *Biosens Bioelectron.* 2024;268:116860.
 14. Woo K, Santamaria N, Beeckman D, Alves P, Cullen B, Gefen A, Lázaro-Martínez JL, Lev-Tov H, Najafi B, Sharpe A, Swanson T. Using patient-reported experiences to inform the use of foam dressings for hard-to-heal wounds: perspectives from a wound care expert panel. *J Wound Care.* 2024;33(11):814–22.
 15. Xing X, Liu C, Zheng L. Preparation of photo-crosslinked microalgae-carboxymethyl Chitosan composite hydrogels for enhanced wound healing. *Carbohydr Polym.* 2025;348:1122803. (Pt A).
 16. Spicer CD. Hydrogel scaffolds for tissue engineering: the importance of polymer choice. *Polym Chem.* 2020;11(2):184–219.
 17. Wu X-Y, Yang J, Wu F-H, Cao W-B, Zhou T, Wang Z-Y, Tu C-X, Gou Z-R, Zhang L, Gao C-Y. A macroporous cryogel with enhanced mechanical properties for osteochondral regeneration in vivo. *Chin J Polym Sci.* 2023;41(1):40–50.
 18. Ge M, Zhu W, Mei J, Hu T, Yang C, Lin H, Shi J. Piezoelectric-Enhanced nanocatalysts trigger neutrophil N1 polarization against bacterial biofilm by disrupting redox homeostasis. *Adv Mater* (2024) e2409633.
 19. Yang Z, Yuan M, Liu B, Ma Z, Ma J, Ma X, Li K, Ma P, Cheng Z, Lin J. Dual-Defect regulated G-C3N4 for piezoelectric catalytic tumor therapy with enhanced efficacy. *Adv Mater* (2025) e2412069.
 20. Wang M, Huang C, Chen Y, Ji Y, Yu DG, Bligh SWA. Medicated tri-layer fibers based on cellulose acetate and Polyvinylpyrrolidone for enhanced antibacterial and wound healing properties. *Carbohydr Polym.* 2025;348:1122856. (Pt A).
 21. Ahmed S, Khan RA, Rashid TU. Cellulose nanocrystal based electrospun nanofiber for biomedical applications-A review. *Carbohydr Polym.* 2025;348:1122838. (Pt A).
 22. Nur MG, Rahman M, Dip TM, Hossain MH, Hossain NB, Baratchi S, Padhye R, Houshyar S. Recent advances in bioactive wound dressings. *Wound Repair Regen* (2024).
 23. Zhao J, Chen L, Ma A, Bai X, Zeng Y, Liu D, Liu B, Zhang W, Tang S. Recent advances in coaxial electrospun nanofibers for wound healing. *Mater Today Bio.* 2024;29:101309.
 24. Huo S, Liu S, Liu Q, Xie E, Miao L, Meng X, Xu Z, Zhou C, Liu X, Xu G. Copper-Zinc-Doped bilayer bioactive glasses loaded hydrogel with Spatiotemporal Immunomodulation supports MRSA-Infected wound healing. *Adv Sci.* 2024;11(5):2302674.
 25. Huo S, Lyu Z, Su X, Wang F, Liu J, Liu S, Liu X, Bao X, Zhang J, Zheng K. Formation of a novel Cu-containing bioactive glass nano-topography coating with strong bactericidal capability and bone regeneration. *Compos Part B: Eng.* 2023;253:110521.
 26. Yang N, Shi N, Yao Z, Liu H, Guo W. Gallium-modified gelatin nanoparticles loaded with Quercetin promote skin wound healing via the regulation of bacterial proliferation and macrophage polarization. *Front Bioeng Biotechnol.* 2023;11:1124944.
 27. Guo Z, Ge M, Ruan Z, Ma Y, Chen Y, Lin H. 2D Janus carrier-enabled Trojan horse: gallium delivery for the sequential therapy of biofilm associated infection. *Biomaterials.* 2024;313:122761.
 28. Lan Z, Guo L, Fletcher A, Ang N, Whitfield-Cargile C, Bryan L, Welch S, Richardson L, Cosgriff-Hernandez, antimicrobial hydrogel foam dressing with controlled release of gallium maltolate for infection control in chronic wounds. *Bioact Mater.* 2024;42:433–48.
 29. Huo S, Wang F, Lyu Z, Hong Q, Nie Be, Wei J, Wang Y, Zhang J, Yue B. Dual-functional polyetheretherketone surface modification for regulating immunity and bone metabolism. *Chem Eng J.* 2021;426:130806.
 30. Lei J, Wang C, Feng X, Ma L, Liu X, Luo Y, Tan L, Wu S, Yang C. Sulfur-regulated defect engineering for enhanced ultrasonic piezocatalytic therapy of bacteria-infected bone defects. *Chem Eng J.* 2022;435:134624.
 31. Wu M, Zhang Z, Liu Z, Zhang J, Zhang Y, Ding Y, Huang T, Xiang D, Wang Z, Dai Y, Wan X, Wang S, Qian H, Sun Q, Li L. Piezoelectric nanocomposites for sonodynamic bacterial elimination and wound healing. *Nano Today.* 2021;37:101104.
 32. Bonadies I, Longo A, Androsch R, Jehnichen D, Göbel M, Di Lorenzo ML. Biodegradable electrospun PLLA fibers containing the mosquito-repellent DEET. *Eur Polymer J.* 2019;113:377–84.
 33. Pimentel ES, Brito-Pereira R, Marques-Almeida T, Ribeiro C, Vaz F, Lanceros-Mendez S, Cardoso VF. Tailoring electrospun Poly (L-lactic acid) nanofibers as substrates for microfluidic applications. *ACS Appl Mater Interfaces.* 2019;12(1):60–9.
 34. Shang L, Huang Z, Pu X, Yin G, Chen X. Preparation of graphene oxide-doped polypyrrole composite films with stable conductivity and their effect on the elongation and alignment of neurite. *ACS Biomaterials Sci Eng.* 2019;5(3):1268–78.
 35. Song J, Zhang B, Lu Z, Xin Z, Liu T, Wei W, Zia Q, Pan K, Gong RH, Bian L. Hierarchical porous Poly (l-lactic acid) nanofibrous membrane for ultrafine particulate aerosol filtration. *ACS Appl Mater Interfaces.* 2019;11(49):46261–8.
 36. Niemczyk-Soczynska B, Gradys A, Sajkiewicz P. Hydrophilic surface functionalization of electrospun nanofibrous scaffolds in tissue engineering. *Polym (Basel)* 12(11) (2020).
 37. Fernández-Hernández S, Gil J, Robles-Cantero D, Pérez-Pevida E, Herrero-Climent M, Brizuela-Velasco A. Influence of the sodium titanate crystal size of biomimetic dental implants on osteoblastic behavior: an in vitro study. *Biomimetics (Basel)* 10(1) (2025).
 38. Zhang Z, He D, Wang X, Ma X, Zheng Y, Gu X, Li Y. In vitro and in vivo evaluation of osteogenesis and antibacterial activity of MgGa alloys. *Acta Biomater.* 2024;185:85–97.
 39. Sun Y, Liu J, Chen K, Zhong N, He C, Luan X, Zang X, Sun J, Cao N, Wang W, Ren Q. Polydopamine grafting polyether ether ketone to stabilize growth factor for efficient osteonecrosis repair. *Sci Rep.* 2025;15(1):3697.
 40. Wang F, Li S, Wang X, Yang Q, Duan J, Yang Y, Mu H. Gellan gum-based multifunctional hydrogel with enduring sterilization and ROS scavenging for infected wound healing. *Int J Biol Macromol* (2024) 136888.
 41. Guo Z, Ge M, Ruan Z, Ma Y, Chen Y, Lin H. 2D Janus carrier-enabled Trojan horse: gallium delivery for the sequential therapy of biofilm associated infection. *Biomaterials.* 2025;313:122761.
 42. He J, Lin X, Zhang D, Hu H, Chen X, Xu F, Zhou M. Wake biofilm up to enhance suicidal uptake of gallium for chronic lung infection treatment. *Biomaterials.* 2024;310:122619.
 43. Goss CH, Kaneko Y, Khoo L, Anderson GD, Ravishankar S, Aitken ML, Lechtzin N, Zhou G, Czyz DM, McLean K, Olakanmi O, Shuman HA, Teresi M, Wilhelm E, Caldwell E, Salipante SJ, Hornick DB, Siehnel RJ, Becker L, Britigan BE, Singh PK. Gallium disrupts bacterial iron metabolism and has therapeutic effects in mice and humans with lung infections. *Sci Transl Med* 10(460) (2018).
 44. Han ZY, Fu ZJ, Wang YZ, Zhang C, Chen QW, An JX, Zhang XZ. Probiotics functionalized with a gallium-polyphenol network modulate the intratumor microbiota and promote anti-tumor immune responses in pancreatic cancer. *Nat Commun.* 2024;15(1):7096.
 45. Cetin FN, Mignon A, Van Vlierberghe S, Kolouchova K. Polymer- and Lipid-Based nanostructures serving wound healing applications: A review. *Adv Healthc Mater* (2024) e2402699.
 46. Chen SK, Liu JJ, Wang X, Luo H, He WW, Song XX, Yin JY, Nie SP. Self-assembled near-infrared-photothermal antibacterial hericium erinaceus β -glucan/

- tannic acid/Fe (III) hydrogel for accelerating infected wound healing. *Carbohydr Polym.* 2025;348:122898. (Pt B).
47. Ye Y, Zheng Q, Wang Z, Wang S, Lu Z, Chu Q, Liu Y, Yao K, Wei B, Han H, Chen H, Zhang X. Metal-phenolic nanoparticles enhance low temperature photo-thermal therapy for bacterial biofilm in superficial infections. *J Nanobiotechnol.* 2024;22(1):713.
 48. Chen M, Wang J, Zhang P, Jiang Z, Chen S, Liang S, Ma T, Liao H, Tan W, Niu C, Wang L. Low molecular weight fucoidan induces M2 macrophage polarization to attenuate inflammation through activation of the AMPK/mTOR autophagy pathway. *Eur J Pharmacol.* 2024;986:177134.
 49. Zhou R, Huang J, Zhang W, Wang W, Peng W, Chen J, Yu C, Bo R, Liu M, Li J. Multifunctional hydrogel based on Polyvinyl alcohol/chitosan/metal polyphenols for facilitating acute and infected wound healing. *Mater Today Bio.* 2024;29:101315.
 50. Gopee NH, Winheim E, Olabi B, Admane C, Foster AR, Huang N, Botting RA, Torabi F, Sumanaweera D, Le AP, Kim J, Verger L, Stephenson E, Adão D, Ganier C, Gim KY, Serdy SA, Deakin C, Goh I, Steele L, Annusver K, Miah MU, Tun WM, Moghimi P, Kwakwa KA, Li T, Basurto Lozada D, Rumney B, Tudor CL, Roberts K, Chipampe NJ, Sidhpura K, Englebert J, Jardine L, Reynolds G, Rose A, Rowe V, Pritchard S, Mulas I, Fletcher J, Popescu DM, Poyner E, Dubois A, Guy A, Filby A, Lisgo S, Barker RA, Glass IA, Park JE, Vento-Tormo R, Nikolova MT, He P, Lawrence JEG, Moore J, Ballereau S, Hale CB, Shanmugiah V, Horsfall D, Rajan N, McGrath JA, O'Toole EA, Treutlein B, Bayraktar O, Kasper M, Prokatzky F, Mazin P, Lee J, Gambardella L, Koehler KR. S.A. Teichmann, M. Haniffa, A prenatal skin atlas reveals immune regulation of human skin morphogenesis. *Nature* (2024).
 51. Zhou S, Tu Z, Chen Z, Jiang D, Lv S, Cui H. Engineering Ga-doped mesoporous bioactive glass-integrated PEEK implants for immunomodulatory and enhanced osseointegration effects. *Colloids Surf B.* 2025;245:114189.
 52. Chen J, Liu Y, Cheng G, Guo J, Du S, Qiu J, Wang C, Li C, Yang X, Chen T, Chen Z. Tailored hydrogel delivering Niobium carbide boosts ROS-Scavenging and antimicrobial activities for diabetic wound healing. *Small.* 2022;18(27):2201300.
 53. Kharaziha M, Baidya A, Annabi N. Rational design of Immunomodulatory hydrogels for chronic wound healing. *Adv Mater.* 2021;33(39):2100176.
 54. Bao X, Huo S, Wang Z, Yang S, Dou L, Liu Y, Huang J, Cai C, Fang B, Xu G. Multifunctional biomimetic hydrogel dressing provides anti-infection treatment and improves immunotherapy by reprogramming the infection-related wound microenvironment. *J Nanobiotechnol.* 2024;22(1):80.
 55. Bi S, He C, Zhou Y, Liu R, Chen C, Zhao X, Zhang L, Cen Y, Gu J, Yan B. Versatile conductive hydrogel orchestrating neuro-immune microenvironment for rapid diabetic wound healing through peripheral nerve regeneration. *Biomaterials.* 2024;314:122841.
 56. Yang Y, Fan L, Jiang J, Sun J, Xue L, Ma X, Kuai L, Li B, Li Y. M2 macrophage-polarized anti-inflammatory microneedle patch for accelerating biofilm-infected diabetic wound healing via modulating the insulin pathway. *J Nanobiotechnol.* 2024;22(1):489.
 57. Kim H, Wang SY, Kwak G, Yang Y, Kwon IC, Kim SH. Exosome-Guided phenotypic switch of M1 to M2 macrophages for cutaneous wound healing. *Adv Sci.* 2019;6(20):1900513.
 58. Ding X, Xie S, Zhang W, Zhu Y, Xu D, Xian S, Sun H, Guo X, Li Y, Lu J, Tong X, Huang R, Ji S, Xia Z. Current application of tissue-engineered dermal scaffolds mimicking the extracellular matrix microenvironment in wound healing. *Regen Ther.* 2025;28:371–82.
 59. Hashemi SS, Sanati P, Rafati A. The inducing effect of epidermal growth factor on acellular dermal matrix in a rat model of skin regeneration. *J Wound Care.* 2025;34(2):137–45.
 60. Zhang S, Gatsi B, Yao X, Jin Y, Amhal H. Cellulose nanofiber-reinforced antimicrobial and antioxidant multifunctional hydrogel with self-healing, adhesion for enhanced wound healing. *Carbohydr Polym.* 2025;352:123189.

Publisher's note

Springer Nature remains neutral with regard to jurisdictional claims in published maps and institutional affiliations.